JGR Solid Earth

RESEARCH ARTICLE
10.1029/2021JB023376

Special Section:
Understanding and anticipating Induced Seismicity: from mechanics to seismology

Coupled Poroelastic Modeling of Hydraulic Fracturing-Induced Seismicity: Implications for Understanding the Post Shut-In M_L 2.9 Earthquake at the Preston New Road, UK

Wenzhuo Cao[1,2], James P. Verdon[3], and Ming Tao[4]

[1]Department of Earth Science and Engineering, Royal School of Mines, Imperial College London, London, UK, [2]Key Laboratory of Deep Earth Science and Engineering, Sichuan University, Chengdu, China, [3]School of Earth Sciences, University of Bristol, Bristol, UK, [4]School of Resources and Safety Engineering, Central South University, Changsha, China

Key Points:

- A coupled poroelastic model considering hydrofracturing-induced pressure perturbations was developed to evaluate induced seismicity
- The post shut-in M_L 2.9 earthquake at the Preston New Road, UK was triggered by pore pressure diffusion to a conductive fault
- The causal mechanism of induced seismicity highly depends on fault permeability and its connectivity to injection regions

Supporting Information:

Supporting Information may be found in the online version of this article.

Correspondence to:

W. Cao,
w.cao15@imperial.ac.uk

Citation:

Cao, W., Verdon, J. P., & Tao, M. (2022). Coupled poroelastic modeling of hydraulic fracturing-induced seismicity: Implications for understanding the post shut-in M_L 2.9 earthquake at the Preston New Road, UK. *Journal of Geophysical Research: Solid Earth*, *127*, e2021JB023376. https://doi.org/10.1029/2021JB023376

Received 8 OCT 2021
Accepted 16 FEB 2022

Author Contributions:

Conceptualization: Wenzhuo Cao
Formal analysis: Wenzhuo Cao
Investigation: Wenzhuo Cao
Methodology: Wenzhuo Cao, Ming Tao
Resources: James P. Verdon
Software: Wenzhuo Cao
Writing – original draft: Wenzhuo Cao

Abstract Post-injection seismicity associated with hydraulic stimulation has posed great challenges to hydraulic fracturing operations. This work aims to identify the causal mechanism of the post shut-in M_L 2.9 earthquake in August 2019 at the Preston New Road, UK, amongst three plausible mechanisms, that is, the post shut-in pore pressure diffusion, poroelastic stressing on a non-overpressurized fault, and poroelastic stressing on an overpressurized fault. A 3D fully coupled poroelastic model that considers the poroelastic solid deformation, fluid flow in both porous rocks and fracture structures, and hydrofracturing-induced pressure perturbations was developed to simulate the hydromechanical response of the shale reservoir formation to hydraulic fracturing operations at the site. Based on the model results, Coulomb stress changes and seismicity rate were further evaluated on the PNR-2 fault responsible for the earthquake. Model results have shown that increased pore pressure plays a dominant role in triggering the fault slippage, although the poroelastic stress may have acted to promote the slippage. Amongst the three plausible mechanisms, the post shut-in pore pressure diffusion is the most favored in terms of Coulomb stress change, seismicity rate, timing of fault slippage and rupture area. The coupled modeling results suggested that the occurrence of the post shut-in M_L 2.9 earthquake was a three-staged process, involving first propagation of fracture tips that stimulated surrounding reservoir formations, then hydraulic connection with and subsequent pore pressure diffusion to the conductive PNR-2 fault, and eventually fault activation primarily under the direct impact of increased pore pressure.

Plain Language Summary Hydraulic fracturing operations at the Preston New Road, UK caused a sequence of induced seismicity, with the largest magnitude 2.9 earthquake occurring after the fracturing operations stopped. The source of this earthquake was identified as a fault structure well oriented to rupture. However, it is unclear whether the fault slippage was primarily caused by direct fluid pressure increase on the fault, stress perturbations generated by injected fluids, or the combined effects of the two. We used computer modeling to simulate the hydrofracturing-induced pressure perturbations, fluid pressure diffusion and associated stress changes during and after hydraulic fracturing operations at the site. Based on simulated stress and pressure fields, we evaluated the potential for fault slippage and relative seismicity counts on the fault identified. Model results have shown that the occurrence of the earthquake is predominantly attributed to increased fluid pressure on the fault after fluid injection, although stress perturbations generated by injected fluids may have contributed to fault rupture. Our findings suggest that the fracturing operations drove hydraulic fractures to impinge on the fault, which was conductive and allowed gentle fluid pressure diffusion to the fault after injection stopped, ultimately leading to the occurrence of the magnitude 2.9 earthquake.

1. Introduction

Hydraulic fracturing has proved to be an effective technique to commercially exploit oil and gas resources from low-permeability reservoirs that are otherwise considered uneconomical. This technique involves the pumping of pressurized fluids into the subsurface to create a fracture network that acts as a permeable channel to increase the production of hydrocarbons from low-permeability formations. However, hydraulic fracturing operations in some formations have faced major challenges in terms of induced seismicity (Atkinson et al., 2020; Schultz et al., 2020). High pressurized fluids have the potential to activate pre-existing fractures/faults, either directly or indirectly, which results in induced seismicity, with moderate-size earthquakes that have been felt at the surface. Regulators have responded to induced seismicity concerns by imposing Traffic Light System (TLS) mitigation

Writing – review & editing: James P. Verdon, Ming Tao

schemes (e.g., Verdon & Bommer, 2021) in some jurisdictions, which have resulted in the suspension or termination of operations at several different sites around the world (Schultz et al., 2020).

In the majority of field sites that have been affected by induced seismicity, the seismicity rate peaks during the hydraulic stimulation stage, followed by diminished level of seismicity after completion of the well (Schultz et al., 2020). However, it is not uncommon for seismicity to persist for days or even months during the shut-in phase, and this is thus referred to as the "trailing effect." For a number of hydraulic fracturing cases, in both shale gas development and enhanced geothermal systems (EGS), the largest earthquake has also occurred after cessation of fluid injection. Examples of hydraulic fracturing operations with significant trailing effects include the South Sichuan Basin, China (Lei et al., 2019) and Preston New Road, UK (Kettlety & Verdon, 2021); examples of EGS sites include Soultz-sous-Forêts, France (Evans et al., 2005), Basel, Switzerland (Häring et al., 2008), Paralana, Australia (Albaric et al., 2014), and Pohang, Korea (Grigoli et al., 2018). The trailing effect poses a challenge to the management of seismic risk using TLSs (Verdon & Bommer, 2021), since they represent a retroactive measure (operations are ceased after an event of a given magnitude).

The use of maximum seismic magnitude forecasting models provide an alternative to TLSs for induced seismicity mitigation (e.g., N.-T. Cao et al., 2020; Clarke, Verdon, et al., 2019; Kwiatek et al., 2019; McGarr, 2014; Si et al., 2020; Verdon & Budge, 2018). These models relate the cumulative seismic moment to the injected volume, and are thus highly dependent on the timely update of operations data. The cessation of fluid injection terminates the monitoring of operations data as model inputs, which impacts the applicability of such models. Regardless of whether TLSs or forecasting models are used, when trailing red light events are detected, few effective mitigation strategies have been identified to alleviate further seismicity, since, by definition, for trailing events the injection has already been stopped.

The driving mechanisms for the trailing effect have not been well understood. Some insights could be obtained by referring to three fundamental mechanisms for induced seismicity: (a) the direct increase in pore pressure (Elsworth et al., 2016; Talwani & Acree, 1985), (b) poroelastic stress perturbations (Segall, 1989; Segall & Lu, 2015), and (c) fault slippage induced stress transfer (W. Cao et al., 2021; Eyre et al., 2019; Guglielmi et al., 2015; Schoenball et al., 2012). The most common explanation for the trailing effect pertains to the delayed effect of pore pressure increase after fluid injection (Baisch et al., 2010; Hsieh & Bredehoeft, 1981; McClure & Horne, 2011; Parotidis et al., 2004). Pore pressure perturbations continue to propagate away from the injection point after the shut-in of the well, which can produce further seismic activity if additional faults are encountered. Another explanation is based on the poroelastic effect caused by fluid injection (Segall & Lu, 2015). Under certain circumstances where injection-induced poroelastic stresses inhibit slip, the abrupt shut-in would cause relaxation of poroelastic stresses, and in turn heightened seismic activity. Poroelastic coupled modeling results of injection-induced fault slippage have suggested that the poroelastic effect could lead to a surge in the post-injection seismicity rate, and that the permeability of faults and hydraulic connectivity of faults are crucial factors governing this process (Chang et al., 2018; Chang & Segall, 2016). As a second-order triggering effect, the stress transfer through aseismic creep subjected to delayed pore pressure diffusion may also play a crucial role in triggering trailing events (Eyre et al., 2020). Elevated pore pressure results in stable sliding on a fault, and subsequently co-seismic slippage of unstable regions. The persistent stable sliding of the fault and continuous loading on unstable regions account for the long-lived nature of post-injection seismic swarms. It was also argued that a large volume of seismic swarms previous linked to fluid diffusion can be alternatively explained by aseismic slip (Eyre et al., 2020).

In additions to explanations based on the three fundamental mechanisms for induced seismicity, a number of novel hypotheses that consider the shut-in conditions have also been proposed. One alternative explanation is that pressurized fluids in dead-end fractures backflow into larger fractures during the shut-in phase, potentially generating even larger events than those occurred during injection (McClure, 2015). Ucar et al. (2017) attributed the sustained post-injection seismicity to the normal closure of fractures after ceasing the injection, which acts as a fluid pressure support to advance the pressure front away from the injection point, increase apertures of fractures beyond the near-well region, and cause seismic events. It has also been recognized that the superposition of various mechanisms, such as the direct fluid pressure increase, stress transfer through fault slippage, and thermal effects (primarily in EGS) may have contributed to the persistent post-injection seismicity (De Simone et al., 2017). Some faults may tend to be destabilized by mechanical and thermal effects but held stable by the hydraulic effect during injection. The abrupt termination of injection resulting in sudden pore pressure decrease

may trigger such faults to rupture. The various response times of reservoir formations to hydraulic, mechanical and thermal effects further complicate the variations of the superposed stress field and the fault stability.

The identification of causal mechanisms for post shut-in seismicity usually requires integrated interpretations of geophysical observations, hydrological properties and the geomechanical response. However, insufficient field monitoring data and large uncertainties in hydrological and geomechanical properties often impede such efforts. It is also difficult to preclude the possibility that more than one mechanism is at play in complex geological settings and fault orientations. Nevertheless, certain characteristics of post-injection seismicity may help identify or at least constrain the plausible mechanisms involved in field observations. For example, the delayed occurrence of post shut-in seismicity favors the delayed pore pressure diffusion mechanism or the aseismic slippage stress transfer mechanism, whereas the immediate post-injection occurrence and long distance away from the injection region indicate the poroelastic stressing mechanism. Some features may be difficult to explain with the delayed pore pressure diffusion mechanism, such as prolonged duration (up to several months), steady seismicity rate over time, and lack of hypocenter migration, indicate a role for the aseismic slippage stress transfer mechanism (Eyre et al., 2020). Seismicity event locations that are beyond previously stimulated regions (e.g., in Basel and Paralana) may suggest one or more of the delayed pore pressure diffusion mechanism, aseismic slip stress transfer mechanism, and post-injection fracture normal closure mechanism. So far, the delayed pore pressure diffusion mechanism has been considered as the primary driving mechanism for post-injection seismicity in several hydraulic fracturing sites, for example, the South Sichuan Basin, China (Lei et al., 2019), and the Red Deer region in Alberta, Canada (Wang et al., 2020). The aseismic slip mechanism was favored to explain the persistent post-injection seismicity in the Fox Creek region in Alberta, Canada (Eyre et al., 2020). Field observations of other recent novel hypotheses have not yet been reported.

Building upon different causal mechanisms of trailing events, various countermeasures have been proposed to mitigate against seismic risk. For example, in regards to the poroelastic stressing mechanism, tapering fluid injection rate instead of abrupt termination upon shut-in could lower or even eliminate the post shut-in spike in seismicity (Segall & Lu, 2015). Concerning the fluid backflow from dead-end fractures mechanism, reducing wellhead pressure (by initiating flowback immediately after injection) may be effective in alleviating post shut-in earthquakes (McClure, 2015).

In this work, the causal mechanism for a post shut-in M_L 2.9 earthquake at the Preston New Road, UK, has been investigated through coupled poroelastic modeling that considers poroelastic solid deformation, fluid flow in both porous rocks and fault structures, and hydrofracturing-induced pressure perturbations. A recent work by Kettlety and Verdon (2021), where elastostatic stress modeling was performed under a representative ambient stress field, has suggested that this earthquake was most likely driven by delayed pore pressure diffusion. The objective of the current work is to reveal the evolving stress, pore pressure and seismicity rate on the activated fault during and after the hydraulic fracturing operations, and to ascertain the respective contribution of delayed pore pressure diffusion and poroelastic stressing toward the post-injection fault slippage. In particular, we have examined three plausible mechanisms for the occurrence of the post shut-in earthquake, that is, the post shut-in pore pressure diffusion, poroelastic stressing on a non-overpressurized fault, and poroelastic stressing on an overpressurized fault. We have also investigated the role of fault permeability and its connectivity to injection regions on the hydromechanical behavior of reservoir formations and associated seismicity on the fault.

2. Post Shut-In M_L 2.9 Earthquake at Preston New Road

In 2011, hydraulic fracturing operations commenced at the Preese Hall site in Lancashire, UK, marking the first onshore shale gas exploration in the UK (Clarke et al., 2014). In 2017, two horizontal wells (PNR-1z and PNR-2) were drilled in preparation for resumption of hydraulic fracturing tests at the Preston New Road (PNR) site, some 2.5 miles from Preese Hall. The PNR-1z well targeted the upper-most section of the Lower Bowland Shale at 2.3 km depth, while the PNR-2 well was drilled approximately 250 m to the north of the PNR-1z well through the lower-most section of the Upper Bowland Shale at 2.1 km depth. A surface monitoring array (broadband seismometers and geophones) and a downhole geophone array situated in the adjacent well were installed to monitor microseismicity associated with fracturing operations. All operations were regulated by a TLS, where operations would proceed with caution when the seismic magnitude reaches a M_L 0 threshold, and be suspended for a minimum of 24 hr after reaching a M_L 0.5 threshold.

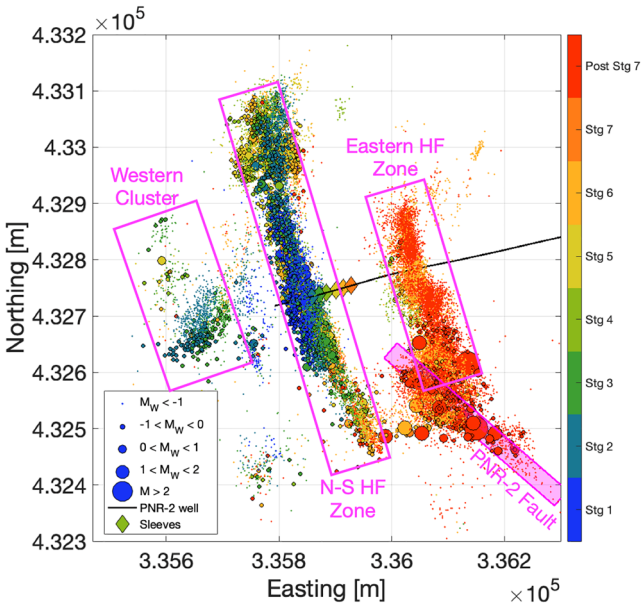

Figure 1. Map view of PNR-2 microseismic event locations (Kettlety et al., 2021). The PNR-2 well path is shown by a black line, and sleeve locations by diamonds colored by stages. Events are sized by magnitude and colored by stages. Coordinates used are based on the Ordnance Survey United Kingdom grid system.

Fracturing operations at the PNR-1z well commenced on 15 October until 17 December 2018 in 16 stages, with a maximum injected volume of 431 m^3 per stage. An M_L 1.1 event occurred at the end of October, which triggered the TLS red light. Operations remained suspended throughout November. Hydraulic fracturing resumed to complete five further injection stages at the heel of the well in December 2018. An M_L 1.6 event occurred during this time, and operations were paused for around 48 hr. Both red light events were believed to be related to a seismogenic planar structure referred to as the PNR-1z fault. The fault geometry was illuminated by microseismic event locations, and the trend of the fault is aligned with the focal mechanisms of the largest events. The microseismic monitoring, processing and interpretation at the PNR-1z well were detailed in Clarke, Soroush, and Wood (2019) and Kettlety et al. (2020).

Hydraulic fracturing at the PNR-2 well took place during the period 15–23 August 2019, which sequentially stimulated seven sleeves evenly spaced at 14.5 m from the toe of the well. The first 6 stages were operated to inject the full volumes of fluids and proppants as planned, with a maximum injected volume of 432 m^3 per stage. After stage 6, seismicity began to escalate and magnitude $M_L > 0.5$ events occurred, resulting in a pause in injection. During stage 7, the well received a reduced volume of injection fluids with increased viscosity to alleviate the risk of seismicity. However, elevated levels of seismicity continued to occur after the end of injection, ultimately culminating in the occurrence of the M_L 2.9 earthquake. The regions stimulated and fault structures activated from the PNR-1z and PNR-2 operations were believed to be hydraulically isolated, since almost no overlap exists between microseismic event locations from the two wells (Kettlety et al., 2021). Here, we focus on the spatiotemporal distribution of induced seismic events including the largest M_L 2.9 earthquake during the PNR-2 operations.

Detailed microseismic interpretation of the PNR-2 microseismicity can be found in Kettlety et al. (2021) and Kettlety and Verdon (2021). We reprise key aspects on that analysis here. In the PNR-2 operations, microseismic events induced during stage 1 formed a cluster extending approximately 50 m above and below the well, and 150 m to the north and south, centered on the injection location. The cluster is closely aligned to the maximum principal stress direction, with a strike of 350° in the northward-propagating segment, and 155° in the southward-propagating one. This cluster was believed to represent the main hydraulic fracture emanating from the PNR-2 well, and was referred to by Kettlety et al. (2021) as the NS Zone (see Figure 1). The NS Zone was driven by stage 2 operation to extend roughly 200 m northwards and 100 m southwards, followed by being maintained over stage 3 and 4 operations. Further to the west of the main NS zone, a cluster containing a smaller number of microseismic events also developed from stage 2 onwards. This cluster generally followed the maximum horizontal principal stress orientation, but manifested as a more diffusive feature. This microseismic cluster was also interpreted to result from hydraulic fracturing, and was referred to as the Western Cluster (see Figure 1) by Kettlety et al. (2021).

After the stage 4 operation had stopped, a new seismogenic zone emerged approximately 100 m to the east of the main NS Zone, and slightly deeper than the well. This cluster with a height of approximately 60 m, gradually propagated around 50 m southwards along the maximum horizontal principal stress orientation. This cluster was believed to represent another hydraulic fracture extending from the PNR-2 well, and was referred to as the Eastern Zone (see Figure 1) by Kettlety et al. (2021). During stages 5 and 6, microseismic events continued to occur within the NS Zone. In addition, the length of the Eastern Zone was extended to approximately 100 m and then to 300 m to both the north and south of the well. Most microseismic events induced during the stage 7 operation were restricted within both the NS and Eastern Zones. Roughly 5 hr after injection of stage 7 had ceased, a sequence of earthquakes of magnitude in excess of M_L 1.0 occurred, including the largest M_L 2.9 earthquake, which occurred 66 hr after the end of stage 7. Kettlety et al. (2021) used the aftershock locations determined from the downhole array to illuminate the fault structure as the source of the M_L 2.9 earthquake. The aftershock cluster

defined a near-vertical seismogenic planar fault measuring 330 × 250 m (length × height), and extending to the southeast of the Eastern Zone (Kettlety et al., 2021). Integrated interpretations of the M_L 2.9 earthquake focal mechanism and the fault plane fitting to the seismic cluster have suggested that the fault has a strike/dip/rake of 135°/80°/180°. This fault was denoted as the PNR-2 fault (see Figure 1).

The fault activation mechanism responsible for the largest earthquakes at the PNR site is of particular interest. Kettlety and Verdon (2021) investigated the fault triggering mechanisms of both PNR-1z and PNR-2 faults through elastostatic stress modeling of the two hydraulic fracturing operations and the spatio-temporal evolution of microseismic event locations. To evaluate the impact of hydraulic fractures on stress conditions in the reservoir formation, they adopted a stochastic hydraulic fracture model, where a population of hydraulic fractures were generated following statistical distributions of fracture geometrical attributes. This modeling approach allowed them to examine median Coulomb stress changes on target faults and the variability from multiple model realizations. It was found that PNR-1z was activated by the compound effects of direct pore pressure increase and stress transfer caused by hydraulic fracture opening. The PNR-2 fault was most likely governed by the post shut-in diffusion of increased pore pressure through hydraulically stimulated regions. However, the stress transfer produced by hydraulic fracturing opening may also have contributed to destabilize the fault. The difference between triggering behavior of the two faults was attributed to the fault orientation in respect to the in-situ stress field: the PNR-1z fault is moderately well oriented to slip, whilst the PNR-2 fault is extremely well orientated to slip.

The elastostatic stress modeling of Kettlety and Verdon (2021) has qualitatively demonstrated the respective contribution of pore pressure change and poroelastic stress toward fault slippage by representing the most representative stress state that would exist during the hydraulic fracturing operations. However, this model did not capture the evolution of the pore pressure and stress state on target faults during the fracturing operations, and more importantly, after the end of injection. In addition, it is still unclear how the respective contribution of pore pressure change and poroelastic stress toward fault slippage varies, depending on the injection stages, stimulated regions, and hydraulic properties of the reservoir. This requires a more complex coupled hydromechanical model that considers both the extent of hydrofracturing-induced pressure perturbations and injection pressure history and in order to reveal the time-varying stress and pore pressure changes on target faults as the hydraulic fractures propagate and the reservoir is stimulated.

3. Coupled Poroelastic Reservoir Model for Hydraulic Fracturing-Induced Seismicity Evaluation

A 3D fully coupled poroelastic model, considering poroelastic solid deformation, fluid flow in both porous rocks and fault structures, and hydrofracturing-induced pressure perturbations, was developed to model the hydromechanical behavior of the shale formation during and after the PNR-2 operations, and to further evaluate the potential for earthquakes on the PNR-2 fault. This section presents the development of the coupled poroelastic reservoir model, with the mathematical formulation of the model provided in Appendix A.

As shown in Figure 2, a 1,000 m-long cubic hydromechanical model was constructed to simulate the PNR-2 hydraulic fracturing operations and the associated hydromechanical response of shale formations. For simplification, the model was considered to be comprised of shale formations with uniform mechanical and hydrological properties. The fluid injection-induced geomechanical response was modeled using the linear elastic constitutive model, with Poisson's ratio $\upsilon = 0.29$, and Young's modulus $E = 25.7$ GPa (Verdon et al., 2020). The matrix permeability of the Bowland Shale was estimated to be typically less than 1×10^{-4} mD (Clarke et al., 2018), therefore, the shale formations at the PNR-2 site were assumed to have a permeability $k = 1 \times 10^{-4}$ mD before stimulation. Generic values were used for other hydrological properties: porosity $\phi = 0.1$, and Biot coefficient = 0.8.

The model comprises of the two main hydraulic fracture zones (NS Zone and Eastern Zone), whose dimensions and orientations were determined based on the microseismic clouds recorded during and after the PNR-2 operation. Although multiple hydraulic fracture branches may be present, these inter-connected fractures were simplified as two major vertical hydraulic fractures, one in each zone. The two major hydraulic fractures, as well as the PNR-2 fault, were represented by single low-dimension layers in the model, as shown in Figure 2. Refined triangular surface meshes with maximum element sizes of 10 and 30 m were created for the PNR-2 fault plane and hydraulic fractures, respectively. The remaining parts were discretized by a free tetrahedral mesh with

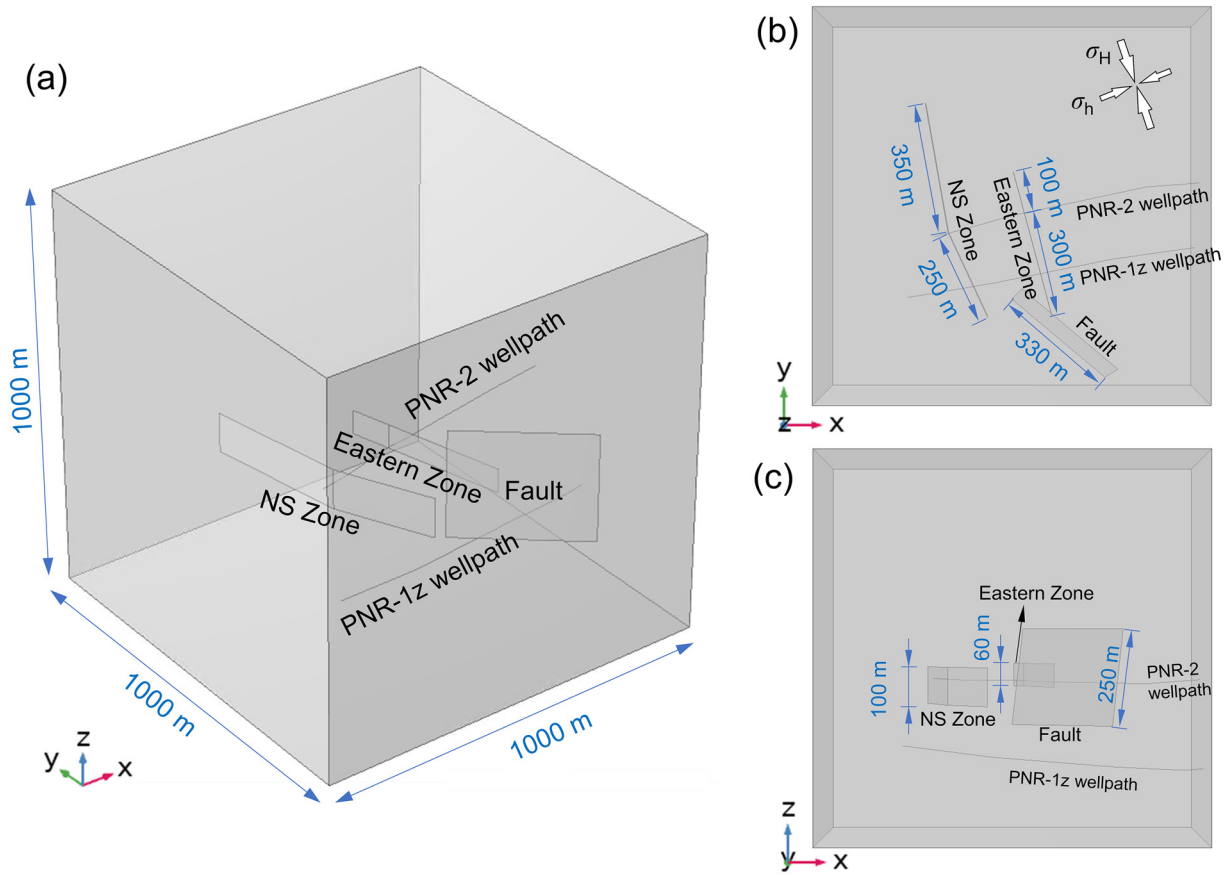

Figure 2. 3D model geometry for hydraulic fracturing operations at the Preston New Road, UK: (a) 3D view, (b) plan view, and (c) side view.

a maximum element size of 100 m, which becomes progressively coarser away from the PNR-2 fault plane and hydraulic fractures.

The tectonic stress at the PNR site is characterized by a strike-slip fault regime. Following the fracture growth trajectories delineated by microseismic clouds, the maximum principal stress was estimated to orient at 173° at the PNR site. The stress gradient of the maximum, intermediate (vertical) and minimum principal stresses are 0.032, 0.026 and 0.017 MPa/m, respectively, and the pore pressure gradient is 0.012 MPa/m (Clarke, Soroush, & Wood, 2019; Verdon et al., 2020). The model was initialized with both the in-situ stress and the initial poroelastic strain caused by the in-situ pore pressure, so as to achieve a uniform initial stress distribution at the same depth before hydraulic fracturing operations begin. The boundary conditions were set up in such a manner that the model base is fixed, and normal and shear stress components calculated from the in-situ stresses were applied to top and lateral boundaries. The initial pore pressure was vertically distributed based on gravitational equilibrium of fluids. Fluid pressures computed from the pressure gradient was applied to all the outer boundaries to reach an initial pore pressure equilibrium.

Fluid pressure perturbations caused by the propagation of the two major hydraulic fractures were modeled in such a way that pressure perturbations initiate upon the onset of hydraulic fracturing operations, followed by progressive extension to the maximum lengths over the fracturing period (Zeng et al., 2021). Considering that microseismicity began to appear along the designated hydraulic fractures during the main stages, hydraulic fractures mainly propagate during and shortly after main stages, when the bottomhole pressure exceeds the minimum principal stress at 2,100 m depth (around 35.7 MPa). For simplicity we assumed that hydraulic fractures only propagate within the main stages of hydraulic fracturing, when the maximum injection rate maintained for a period (Figure 3b, see hydraulic fracture length for northward- and southward-propagating segments of the NS and Eastern Zones in Supporting Information S1). It is acknowledged that hydraulic fractures may propagate sublinearly over time as indicated by analytical solutions such as KGD and PKN models (Rahman & Rahman, 2010).

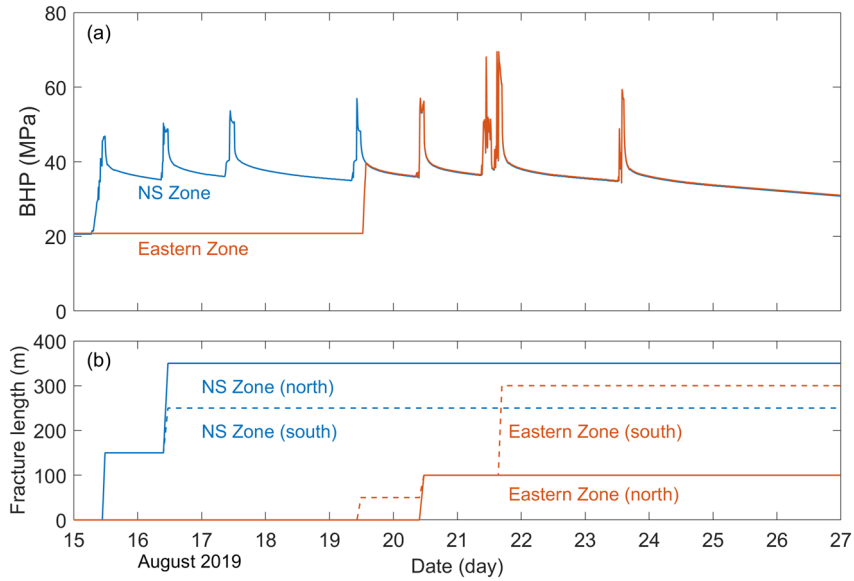

Figure 3. Injection pressure and hydraulic fracture growth histories used to simulate the hydraulic fracturing operations at the Preston New Road, UK: (a) bottomhole pressure history for both NS and Eastern Zones, and (b) hydraulic fracture length for northward- and southward-propagating segments of the NS and Eastern Zones.

Here we assumed a linear approximation and used a constant propagation velocity during each operation stage for simplicity. This model is not intended to accurately simulate the physical process of fracture propagation, but to represent the spatio-temporal overpressure distribution in designated hydraulic fracture paths and its influence on distant fault structures. The permeability of formations adjacent to activated segments of the hydraulic fractures (within a certain stimulated width given later) was elevated from 1×10^{-4} to 100 mD. This was done at each time step such that as the hydraulic fracture propagates, surrounding formations within the specified distance to hydraulic fractures are progressively stimulated.

The interaction of the fault and fractures with bounding formations takes place when the stimulated bounding formations impinge on the PNR-2 fault and establish the hydraulic connection. The hydrological behavior is simulated in such a way that fluid flow in both fractures and porous rock matrix satisfies the conservation of mass, and is linked at the interface by a source term representing the exchange of fluids between the two. Note that we focus on the injection-induced stress changes on the fault and fractures, rather than the fracture/fault displacement and slippage behavior, so only stress perturbations from the porous rock matrix to the fault and fractures were modeled, but not the opposite.

Although the injection ports from the seven injection stages are spaced by 14.5 m, it is believed that hydraulic fracture branches are well connected according to microseismic observations. Thus, fluid injection into the NS and Eastern Zones was modeled by applying overpressure on the two main hydraulic fractures planes, instead of on the respective injection ports along the PNR-2 wellpath. The bottomhole pressure history at the fracturing depth back calculated from the wellhead pressure history was used as injection pressure inputs (Figure 3a, see the wellhead pressure history for both the NS and Eastern Zones in Supporting Information Data Set S1). The NS Zone initiates since stage 1, and the Eastern Zone is not activated until after stage 4. The field wellhead pressure history was recorded until 25 August, and the bottomhole pressure used after this date evolves with a leak-off type pressure decrease following an exponential function. The use of the injection pressure control in the numerical model allows for the accurate modeling of stress perturbations resulting from fluid injection, while the injection volume, which is not the focus of this work, is not explicitly represented.

To understand the dominating factor of the fault slippage, the fault permeability and its hydraulic connection with injection regions were varied to assess the fault behavior in various scenarios. Two end members of fault permeability, 100 mD and 10^{-6} mD, were considered to represent conductive and sealing fault scenarios in the numerical model. For ease of interpretation, we assume an individual fracture (fault plane) to provide the full effective permeability of the fault zone. The fault permeability was represented by assigning a uniform aperture over the

Table 1
Six Model Scenarios With Various Fault Permeabilities k and Stimulated Widths w

	$k = 100$ mD	$k = 10^{-6}$ mD
$w = 0$ m	Hydraulically isolated conductive fault	Hydraulically isolated sealing fault
$w = 100$ m	Conductive fault hydraulically connected to the Eastern Zone (baseline scenario)	Sealing fault hydraulically connected to the Eastern Zone
$w = 200$ m	Conductive fault hydraulically connected to both the NS and Eastern Zones	Sealing fault hydraulically connected to both the NS and Eastern Zones

PNR-2 fault plane, based on the relationship between the effective fracture permeability k and fracture geometry (fault width h and aperture of fault plane e), given by $k = e^3/(12h)$. Assuming a 10 m wide fault zone, apertures of 0.23 and 0.00049 mm provide effective permeabilities of 100 and 10^{-6} mD, respectively. The hydraulic connection between hydraulic fractures and the PNR-2 fault was varied by controlling the width of hydraulically stimulated regions. We used 0, 100 and 200 m stimulated widths to represent hydraulic isolation of the PNR-2 fault, hydraulic connection only to the Eastern Zone, and hydraulic connection to both the NS and Eastern Zones, respectively. A total of six model scenarios were considered in the model, as listed in Table 1.

The coupled poroelastic model was solved using the finite element method-based software COMSOL Multiphysics. The MUMPS direct solver was used, employing the backward differentiation formulas (BDF) method for time stepping. A maximum timestep of 10 min was used due to accuracy considerations in the fluid flow modeling.

Based on results of the coupled model, the potential for seismicity was further evaluated in terms of the Coulomb failure stress change along vulnerable fracture planes (see Appendix B). The fracture orientation most vulnerable to rupture is $45°-\varphi/2$ (φ is the internal friction angle of reservoir rocks given by $f = \tan\varphi$) off the maximum principal stress direction, according to the Mohr-Coulomb failure criterion. Considering a friction coefficient $f = 0.6$ (Verdon et al., 2020) and the maximum principal stress orientation of 173°N at the PNR site, the most vulnerable fracture plane is orientated at 144.5°N or 202.5°N. The Coulomb failure stress change $\Delta\tau$ in response to hydraulic fracturing was resolved on the PNR-2 fault plane with the fault strike 130°N, which is well oriented to rupture.

To quantify the relative abundance of seismic occurrence at hydraulic fracturing-induced stress conditions, the seismicity rate was examined based on the modeled stress and fluid pressure distribution. The seismicity rate model used correlates the prevailing seismicity rate relative to the background rate with the prevailing Coulomb stressing rate relative to the tectonic stressing rate (see Appendix C). The in-situ effective normal stress at 2,100 m depth at the PNR site is 10.5 MPa. The background stressing rate can be obtained by multiplying the shear modulus of fault rocks by the strain rate derived from GPS measurements of horizontal velocities in the region of investigation (Hager et al., 2021). Due to the absence of GPS measurements at the PNR-2 site, we chose the background stressing rate through fitting modeled cumulative number of seismic events to the field recorded value. Assuming the constitutive parameter $a = 0.005$, the background stressing rate $\dot{\tau}_0$ that yields a satisfactory match is 10^{-3} MPa/yr, such that 1 MPa stress along the fracture plane accumulates in 10^3 years. As a result, a characteristic decay time is $t_a = 52.5$ years. In our model, we assumed that seismicity will only occur in regions with abundant fractures, such as within the NS and Eastern Zones and the PNR-2 fault.

4. Model Results and Analysis

4.1. Poroelastic Response to Hydraulic Fracturing

Before investigating the full problem involving different model scenarios, we illustrate the effect of poroelastic coupling on the reservoir behavior by comparing results of the baseline model scenario from an uncoupled model, a one-way fluid-to-solid coupled model, and a two-way poroelastic coupled model (see Text S1 and Figure S1 in Supporting Information S1). In following sections, numerical results presented are from the two-way poroelastic coupled model.

Figure 4 presents the pore pressure change Δp after injection stages 3 and 7 for the six model scenarios. The increased pore pressure only distributes within stimulated regions in all the scenarios. Whilst the PNR-2 fault is not overpressurized throughout the hydraulic fracturing operations in sealing or isolated fault scenarios, it begins

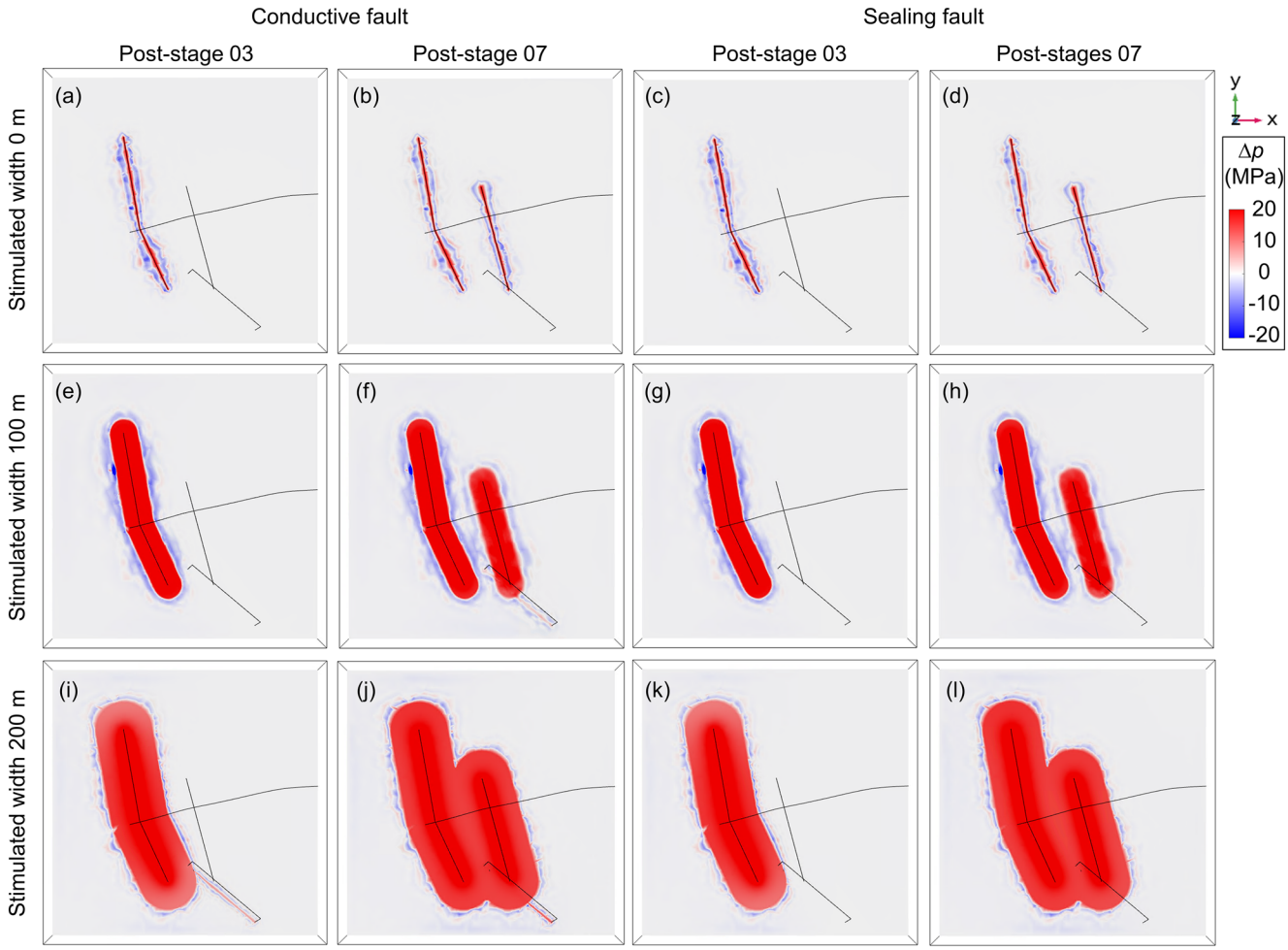

Figure 4. Pore pressure change Δp immediately after injection stages 03 and 07 at 2,100 m depth of the PNR-2 well: (a and b) hydraulically isolated conductive fault, (c and d) hydraulically isolated sealing fault, (e and f) conductive fault hydraulically connected to the Eastern Zone, (g and h) sealing fault hydraulically connected to the Eastern Zone, (i and j) conductive fault hydraulically connected to both the NS and Eastern Zones, and (k and l) sealing fault hydraulically connected to both the NS and Eastern Zones.

to receive fluids as long as the hydraulic fractures impinge on the fault in conductive fault scenarios, such as at stage 7 for 100 m stimulated width (Figure 4f), and at stage 3 for 200 m stimulated width (Figure 4i). The pore pressure diffusion within the stimulated regions forms a pressure gradient, indicating less poroelastic stressing away from the hydraulic fractures. Consequently, the attenuation of pore pressure surrounding stimulated regions due to poroelastic stressing is less apparent for large stimulated widths, in particular a 200 m stimulated width. The normal stress change $\Delta\sigma_n$ and shear stress change $\Delta\tau_s$ after injection stages 3 and 7, along with displacement vectors, are also analyzed for the six model scenarios (see Text 2 and Figures S2 and S3 in Supporting Information S1).

4.2. Coulomb Failure Stress Change

Figure 5 presents the Coulomb failure stress change due to poroelastic stressing $\Delta\tau_s + f\Delta\sigma_n$ after injection stages 3 and 7 for the six model scenarios. The resemblance between Figure 5 and Figure S2 in Supporting Information S1 suggests that the poroelastic stressing effect is dominated by the normal stress changes. In particular, the reduction of normal stress prevails over the elevation of shear stress within the stimulated regions. Nevertheless, strong negative shear stress changes to both sides of the NS and Eastern zones outside the stimulated regions contribute to the inhibition of the potential for fault slippage away from the hydraulic fractures. In isolated or sealing fault scenarios, the northwest end of the PNR-2 fault falls within this seismic inhibited region.

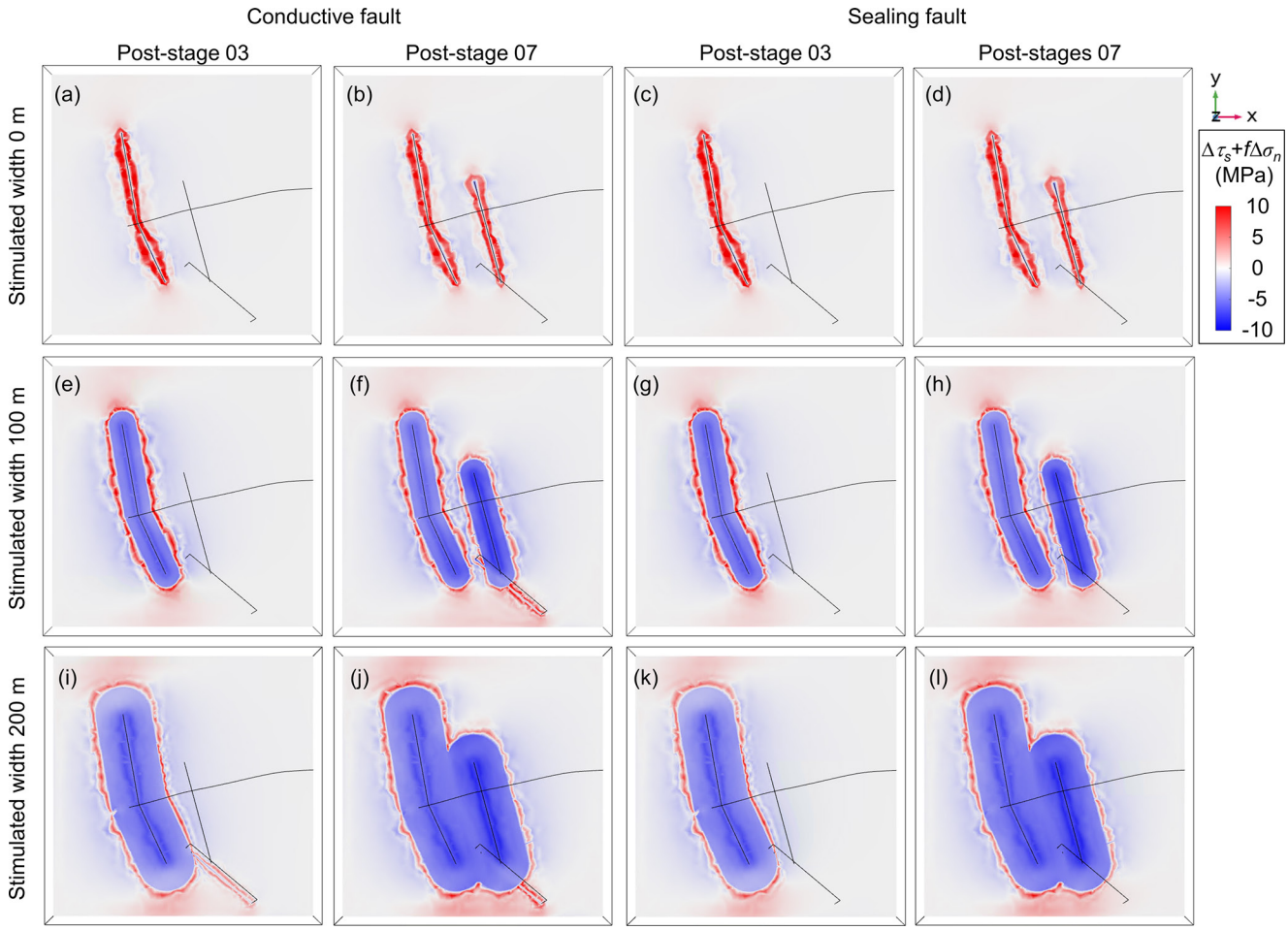

Figure 5. Coulomb failure stress change due to poroelastic stressing $\Delta\tau_s + f\Delta\sigma_n$ immediately after injection stages 03 and 07 at 2,100 m depth of the PNR-2 well: (a and b) hydraulically isolated conductive fault, (c and d) hydraulically isolated sealing fault, (e and f) conductive fault hydraulically connected to the Eastern Zone, (g and h) sealing fault hydraulically connected to the Eastern Zone, (i and j) conductive fault hydraulically connected to both the NS and Eastern Zones, and (k and l) sealing fault hydraulically connected to both the NS and Eastern Zones.

Figure 6 presents the Coulomb failure stress change $\Delta\tau$ after injection stages 3 and 7 for the six model scenarios. The Coulomb failure stress change is dominated by pore pressure change within stimulated regions and the hydraulically connected conductive fault, albeit being restricted by the normal stress change. Outside the stimulated regions, Coulomb failure stress change is primarily contributed by the shear stress change, where the potential for fault slippage is suppressed to the sides of the NS and Eastern zones but promoted at the propagation fronts. In isolated or sealing fault scenarios, the northwest end of the PNR-2 fault is suppressed to slip; but once hydraulic connection is established, the increased pore pressure overwhelms in favor of fault slippage (Figures 6f, 6i and 6j). We further examined the spatial distribution of the Coulomb failure stress change $\Delta\tau$ for the six model scenarios in 3D, and found that injection-induced stress perturbations in the vertical direction quickly fade off away from fractures and the PNR-2 fault (if conductive and hydraulically connected) in all the model scenarios (see Text S3 and Figure S4 in Supporting Information S1).

Figure 7 presents the Coulomb failure stress change $\Delta\tau$ resolved on both hydraulic fracture zones and the PNR-2 fault immediately after each injection stage and at the end of modeling for the six model scenarios. The PNR-2 fault is not stimulated in the isolated fault scenarios (Figures 7a and 7b), which provides a unique case to examine the effect of poroelastic stressing. Since the fluid injection into the NS Zone approaches the PNR-2 fault (at injection stage 02), the northwest end of the fault to the side of the NS Zone is clamped by the increased shear stress. As the Eastern Zone is stimulated (at injection stage 5), the northwest end of the fault in between the NS

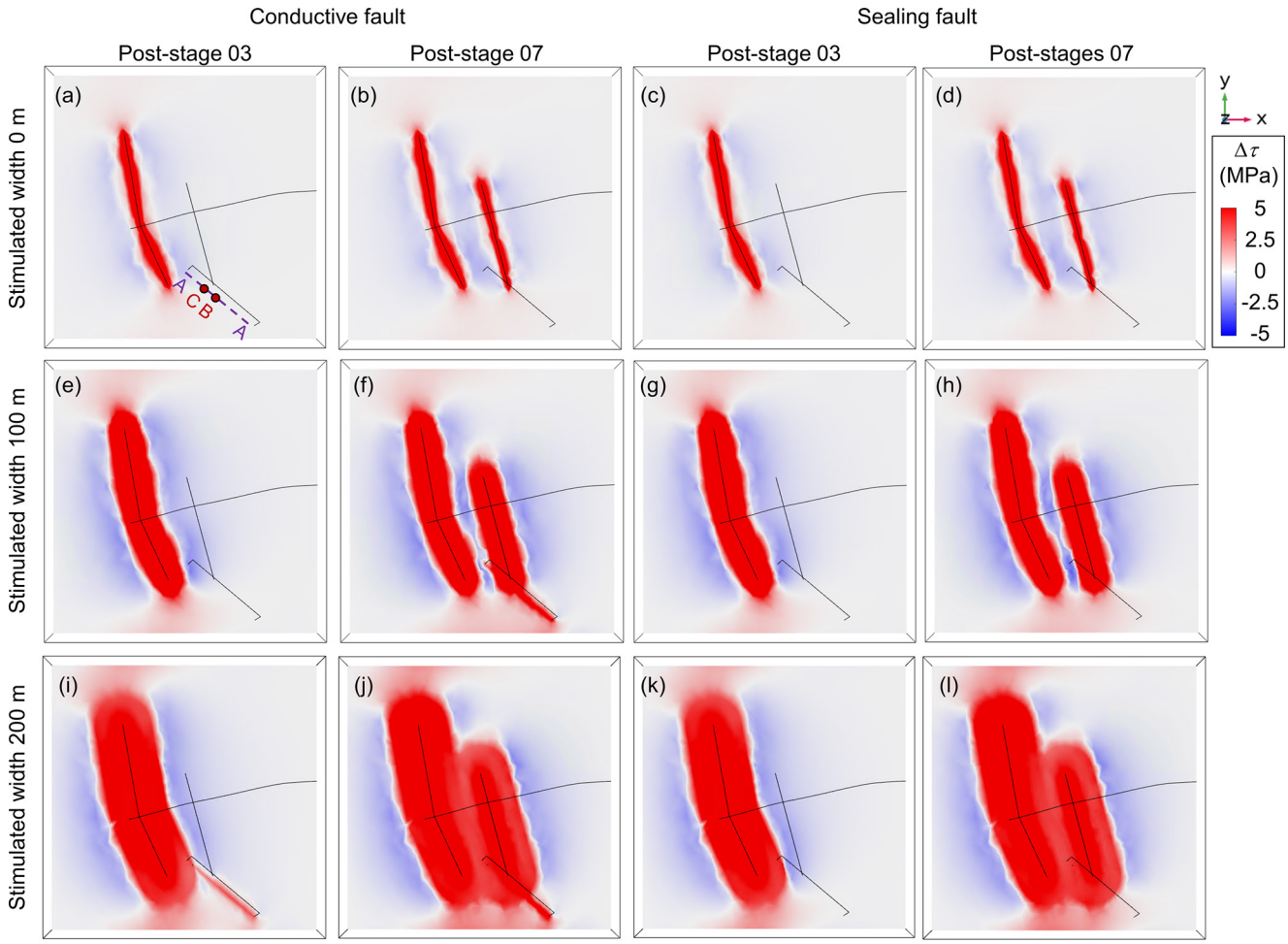

Figure 6. Coulomb failure stress change $\Delta\tau$ immediately after injection stages 03 and 07 at 2,100 m depth of the PNR-2 well: (a and b) hydraulically isolated conductive fault, (c and d) hydraulically isolated sealing fault, (e and f) conductive fault hydraulically connected to the Eastern Zone, (g and h) sealing fault hydraulically connected to the Eastern Zone, (i and j) conductive fault hydraulically connected to both the NS and Eastern Zones, and (k and l) sealing fault hydraulically connected to both the NS and Eastern Zones. In (a), measurement line A-A is set up along the fault strike, and measurement points B and C are set up on the measurement line A-A and spaced by 50 m apart. Point B is on the extension line of the Eastern Zone, and Point C is located within the clamped northwest end of the fault.

and Eastern Zones is further suppressed, whilst the front of Eastern Zone with elevated shear stress impinges on the central part of the fault, promoting the potential for slippage.

When the stimulated width is 100 m (Figures 7c and 7d), the PNR-2 fault is hydraulically connected to the Eastern Zone sometime after injection stage 6. This would intensively drive the entire fault to slip if conductive, or the majority of the fault (except the clamped northwest end) to slip if sealing. Model results for the conductive fault scenario (Figure 7c) present the most satisfactory match to the spatiotemporal distribution of field recorded seismic events. When the stimulated width is 200 m (Figures 7e and 7f), hydraulic connection between the NS Zone and the PNR-2 fault forms sometime after the injection stage 2. A conductive fault would be promoted to slip, whilst a sealing fault would not be promoted until sometime after the injection stage 6, when the Eastern Zone connects with the fault and the stimulated regions cover the majority of the fault.

Comparison between model scenarios with different stimulated widths suggests that the extent of poroelastic stressing is dictated by the area of overpressurized regions, which is in turn influenced by the hydraulic connection of stimulated regions. The larger the stimulated and overpressurized regions, the larger the clamped fault section before hydraulic connection. The Coulomb failure stress change contours in the hydraulically connected sealing fault scenario are consistent with the median Coulomb failure stress change contours influenced by the

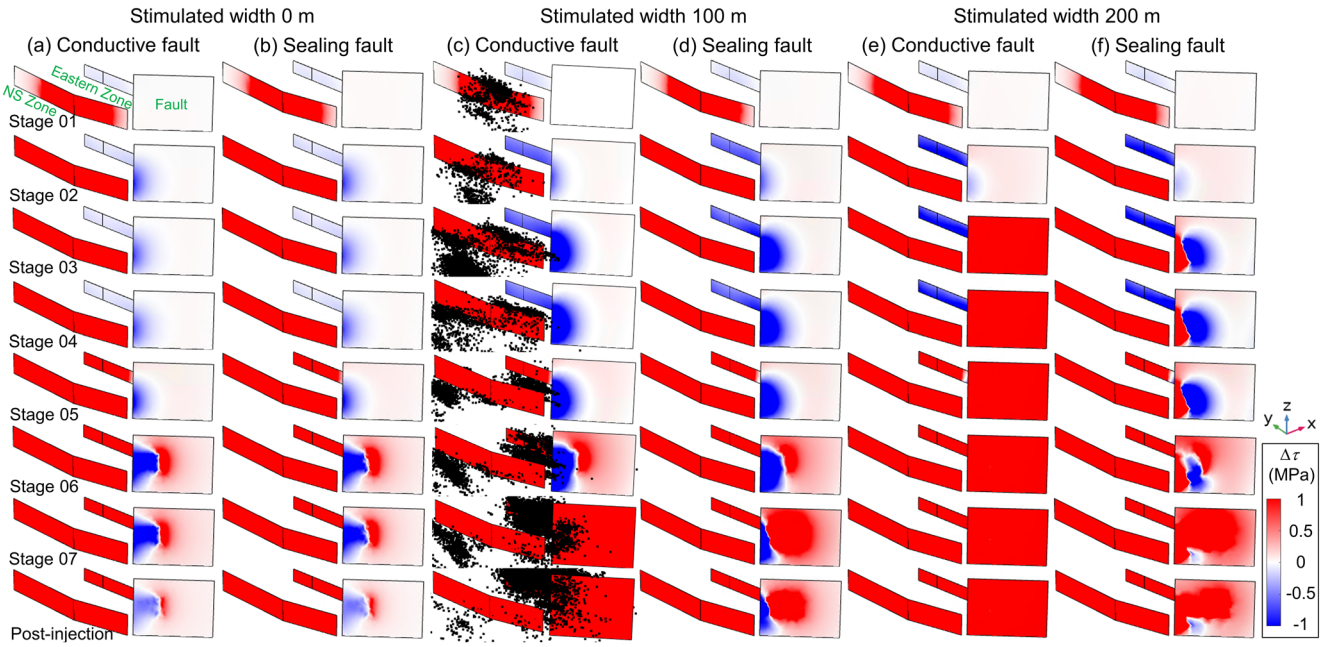

Figure 7. Coulomb failure stress change $\Delta\tau$ on hydraulic fracture planes and the PNR-2 fault plane after each injection stage of the PNR-2 well: (a) hydraulically isolated conductive fault, (b) hydraulically isolated sealing fault, (c) conductive fault hydraulically connected to the Eastern Zone, (d) sealing fault hydraulically connected to the Eastern Zone, (e) conductive fault hydraulically connected to both the NS and Eastern Zones, and (f) sealing fault hydraulically connected to both the NS and Eastern Zones. Field monitored seismic events are marked by black dots in (c).

NS and Eastern Zones, as obtained from previous independent elastostatic stress modeling work incorporating a set of 1,000 stochastic hydraulic fractures for both the NS and Eastern Zones (Kettlety & Verdon, 2021).

To examine the temporal evolution of the Coulomb failure stress change $\Delta\tau$ along the PNR-2 fault, a horizontal measurement line A-A is set up along the fault strike in Figure 6a. As illustrated in Figure 8, poroelastic stressing emerges along the full fault length since the start of the injection, and begins to clamp the northwest end of the fault after stage 2. In hydraulically isolated fault scenarios, the Eastern Zone has a larger influence on Coulomb failure stress changes than the NS Zone (Figures 8a and 8b). If the PNR-2 fault is hydraulically connected to the hydraulic fracture zones, the Coulomb failure stress change $\Delta\tau$ dominated by the pore pressure change could be an order of magnitude larger than that due to poroelastic stressing, either stabilizing or destabilizing. In hydraulically connected sealing fault scenarios, the southeast end of the fault is less influenced by the increased pore pressure (Figures 8d and 8f), as compared to conductive fault scenarios (Figures 8c and 8e). Depending on the overpressure distribution, the extent of the seismicity suppressed fault section is around 150 m for hydraulically isolated fault scenarios (Figures 8a and 8b), but could reach up to 200 m for hydraulically connected sealing fault scenarios (Figures 8d and 8f). The magnitude of Coulomb failure stress change is also the minimum for the hydraulically isolated fault scenarios (Figures 8a and 8b).

To examine the contribution of different stresses toward the Coulomb failure stress change $\Delta\tau$, two measurement points B and C, spaced by 50 m apart, were set up on the measurement line A-A (Figure 6a). Point B is on the extension line of the Eastern Zone, thus would be subjected to the largest positive shear stress change before being hydraulically connected to the Eastern Zone. Point C is located within the clamped northwest end of the fault. Figure 9 presents the stress components at the two measurement points for three different hydraulic connection scenarios. Under injection pressure-controlled conditions, no prominent distinction in hydromechanical behavior was observed between a conductive fault and a sealing fault. In particular, shear stresses in conductive and sealing fault scenarios, respectively marked by yellow solid and dashed lines, are the same in all the graphs, because shear stress is independent of pore pressure change. Notably, when hydraulically connected, a sealing fault characterized by a lower permeability has sharper response to fluid injection than a conductive fault, in terms of both the injection-induced increase and the post-injection decrease in pore pressure change Δp and Coulomb failure stress change $\Delta\tau$ (Figures 9c–9f).

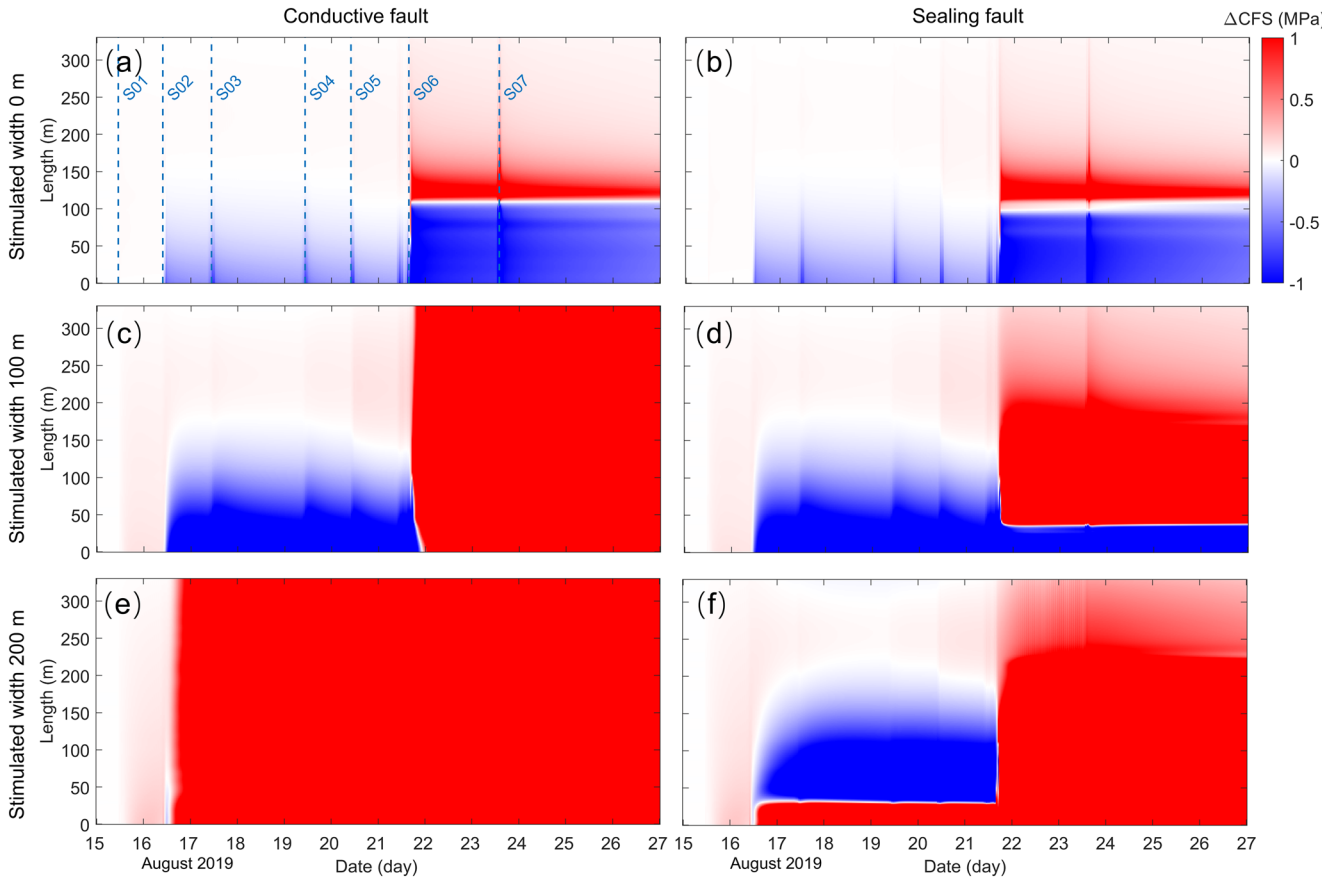

Figure 8. Evolution of Coulomb failure stress change $\Delta\tau$ along the PNR-2 fault plane (the dashed purple line A-A in Figure 6a): (a) hydraulically isolated conductive fault, (b) hydraulically isolated sealing fault, (c) conductive fault hydraulically connected to the Eastern Zone, (d) sealing fault hydraulically connected to the Eastern Zone, (e) conductive fault hydraulically connected to both the NS and Eastern Zones, and (f) sealing fault hydraulically connected to both the NS and Eastern Zones.

In hydraulically isolated fault scenarios, the post-stage 6 C failure stress change $\Delta\tau$ tremendously increases at point B, but sharply decreases at point C (Figures 9a and 9b). The first is attributed to the dominant role of increased shear stress, and the latter to the elevated clamping force. In hydraulically connected scenarios, the elevated pore pressure contributes the most to the potential for fault slippage, although being counteracted by normal stress change in favor of rock compression (Figures 9c–9f). Consequently, points B and C exhibit similar geomechanical behavior. When the fault is conductive and the stimulated width is 200 m, pore pressure change Δp and Coulomb failure stress change $\Delta\tau$ at both points first increase after stage 2, followed by a sudden decease after stage 6 (Figures 9e and 9f). This suggests the hydraulic connection first to the NS Zone where fluid flows to the fault, and then to the Eastern Zone where fluid flows from the fault to the large stimulated regions. The hydraulic connection to the Eastern Zone also greatly enhances the clamping force at both points (Figures 9e and 9f). In contrast, when the fault is not conductive, pore pressure change Δp and Coulomb failure stress change $\Delta\tau$ do not increase until stage 6 at both points.

4.3. Seismicity Rate

Figure 10 presents the seismicity rate R resolved on the PNR-2 fault as well as the hydraulic fracture zones immediately after each injection stage and at the end of modeling for the six model scenarios. Heightened seismic levels are observed in regions with a positive Coulomb stress change $\Delta\tau$, as shown Figure 7. Pore pressure change results in much larger seismicity rates than the poroelastic stress change. In hydraulically isolated scenarios with the poroelastic stressing effect alone, the seismicity rate is mostly limited below 10^4. In contrast, the seismicity rate can reach up to 10^7 in hydraulically connected scenarios where pore pressure change dominates. Due to the quadratic relation between the seismicity rate and its change rate in Equation C1, the Coulomb stress change rate

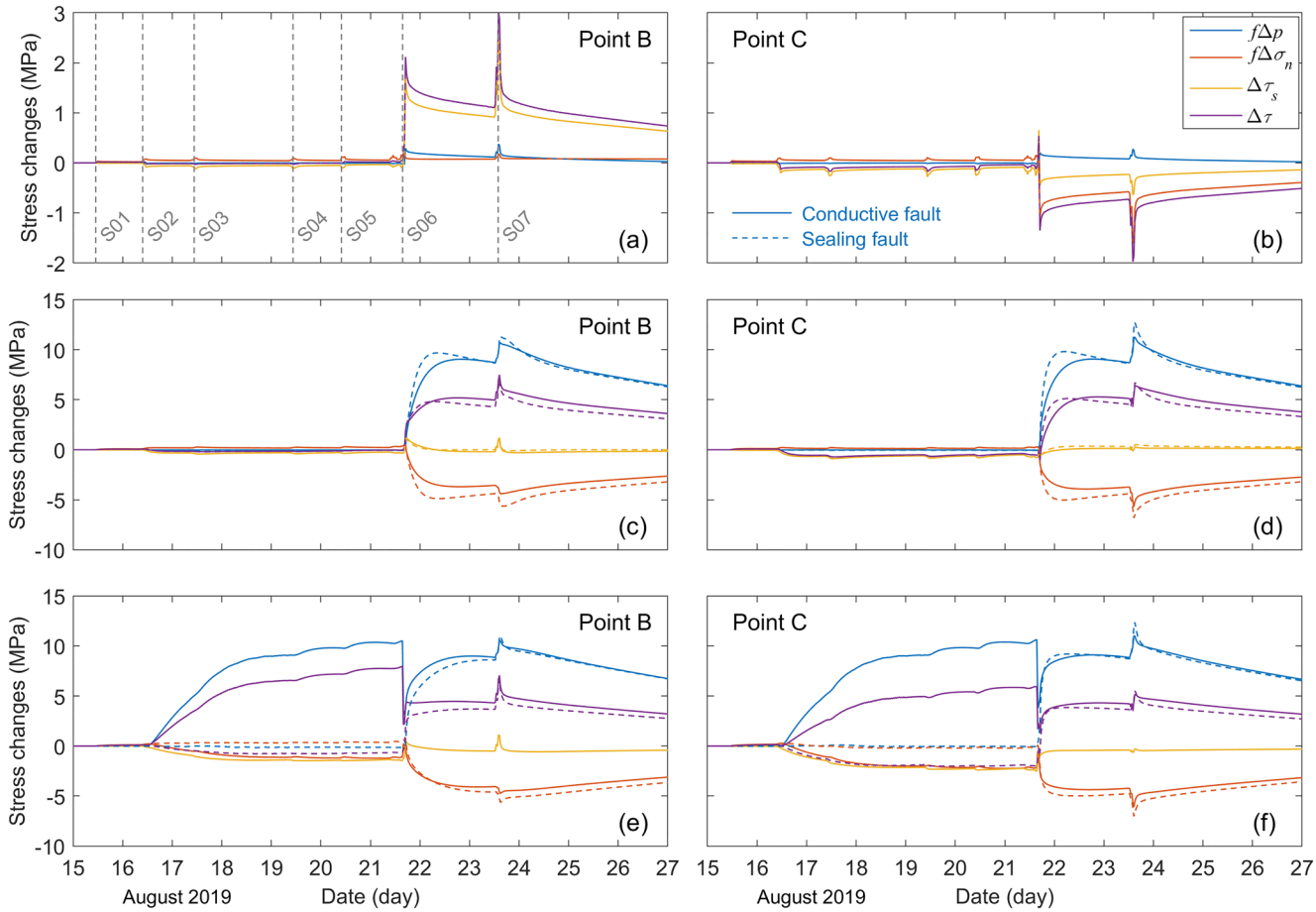

Figure 9. Stress changes at measurement points on the PNR-2 fault: (a) point B (hydraulically isolated fault), (b) point C (hydraulically isolated fault), (c) point B (fault hydraulically connected to the Eastern Zone), (d) point C (fault hydraulically connected to the Eastern Zone), (e) point B (fault hydraulically connected to both the NS and Eastern Zones), and (f) point C (fault hydraulically connected to both the NS and Eastern Zones). Locations of measurement points B and C are shown in Figure 6a.

$\Delta\dot{\tau}$ has a more pronounced effect on the seismicity rate R than on the Coulomb stress change $\Delta\tau$, in particular at high seismicity rates. When the PNR-2 fault is hydraulically connected to the hydraulic fracture zones, the Coulomb stress change $\Delta\tau$ increases by an order of magnitude, but the seismicity rate dramatically increases by over 4 orders of magnitude following the surge in the Coulomb stress change rate $\Delta\dot{\tau}$ (Figures 7 and 10c–10f). Model results for the conductive fault hydraulically connected to the Eastern Zone scenario (Figure 10c) present the most satisfactory match to the spatiotemporal distribution of field recorded seismic events.

Figure 11 presents the seismicity rate evolution along the full fault length over the hydraulic fracturing operation. The temporal evolution of seismicity rate is closely associated with that of the Coulomb stress change shown in Figure 8. Interestingly, although the seismicity rate R surges following a rapid increase in Coulomb stress change rate $\Delta\dot{\tau}$, it does not fade off as fast following a rapid decline in Coulomb stress change rate $\Delta\dot{\tau}$. Each injection stage represents a high Coulomb stress change rate, bringing the seismicity rate to a peak. The Coulomb stress change rate dramatically drops immediately after each injection stage, and the PNR-2 fault is characterized by a steady Coulomb stress only influenced by the pore pressure diffusion process. However, the post-injection seismicity rate has a rapid followed by gentle decline after injection, maintaining at high levels over a prolonged period.

Due to the dominant role of pore pressure change, it can be seen that in hydraulically connected conductive fault scenarios, the maximum heightened seismicity rates spread across the full fault length (Figures 11c and 11e). In contrast, the maximum seismicity rates only concentrate on the most poroelastic stressed fault section for hydraulically isolated fault scenarios (Figures 11a and 11b), and the hydraulically connected fault section for sealing fault scenarios (Figures 11d and 11f). The combined actions of pore pressure change and poroelastic stressing

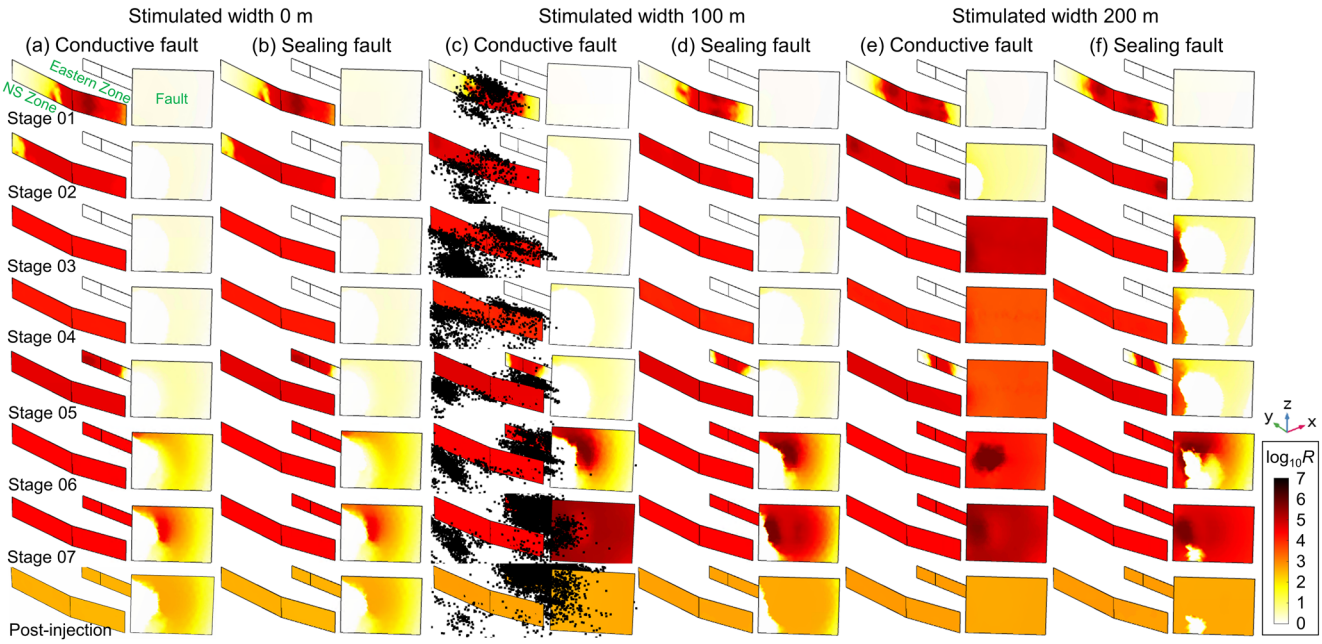

Figure 10. Seismicity rate R on hydraulic fracture planes and the PNR-2 fault plane after each injection stage of the PNR-2 well: (a) hydraulically isolated conductive fault, (b) hydraulically isolated sealing fault, (c) conductive fault hydraulically connected to the Eastern Zone, (d) sealing fault hydraulically connected to the Eastern Zone, (e) conductive fault hydraulically connected to both the NS and Eastern Zones, and (f) sealing fault hydraulically connected to both the NS and Eastern Zones. Field monitored seismic events are marked by black dots in (c).

could also result in variations in seismicity rate distribution along the fault length after injection stage 6, as shown in Figures 11e and 11f.

To compare against field records, the cumulative seismic event count from the baseline model was computed by integrating the mean seismicity rate within the NS and Eastern Zones and the PNR-2 fault over time. The seismicity rate model was calibrated to match field records through tuning two parameters, that is, the background stressing rate to match the time required to reach a steady-state seismicity rate after the onset of injection and post shut-in, and the background seismicity rate to scale the total cumulative event count in the model to the field observed value. Figure 12 presents the comparison between field recorded and modeled cumulative seismic event counts over the hydraulic fracturing operation period. The model prediction achieves an overall satisfactory match to the recorded value, in particular in the first five injection stages. The largest deviation from the field recorded value comes from stage 6, where the model prediction almost overestimates twice the event count. This is believed to be because the bottomhole pressure history estimated from the wellhead pressure history is subject to deviations during hydraulic fracturing. The field wellhead pressure history is characterized by drastic fluctuations related to hydraulic fracturing practices at the PNR site, but the fluctuations may not be immediately reflected in the bottomhole pressure in view of the deep bottomhole level. The bottomhole history used as model inputs for stage 6 has overestimated pressure fluctuations and Coulomb stress change rates, which causes the overestimation of the seismicity rate.

5. Discussion

5.1. Role of Poroelastic Stressing in Triggering Post Shut-In Earthquakes

We proceeded to isolate the contribution of pore pressure change on the Coulomb stress change on the PNR-2 fault. Figures 13a and 13b presents the mean Coulomb stress change $\Delta\tau$ and the contribution from pore pressure change $f\Delta p$ resolved on the PNR-2 fault for the six model scenarios. When both the pore pressure and poroelastic stressing are at play within the PNR-2 fault, such as in hydraulically connected conductive fault scenarios (orange and green lines, Figure 13a), the Coulomb stress change $\Delta\tau$ is lower than the pore pressure change $f\Delta p$. When only the poroelastic stressing effect is active within the PNR-2 fault, such as in hydraulically isolated scenarios (blue lines, Figures 13a and 13b) and sealing fault scenarios (all lines, Figure 13b), the opposite is true. The

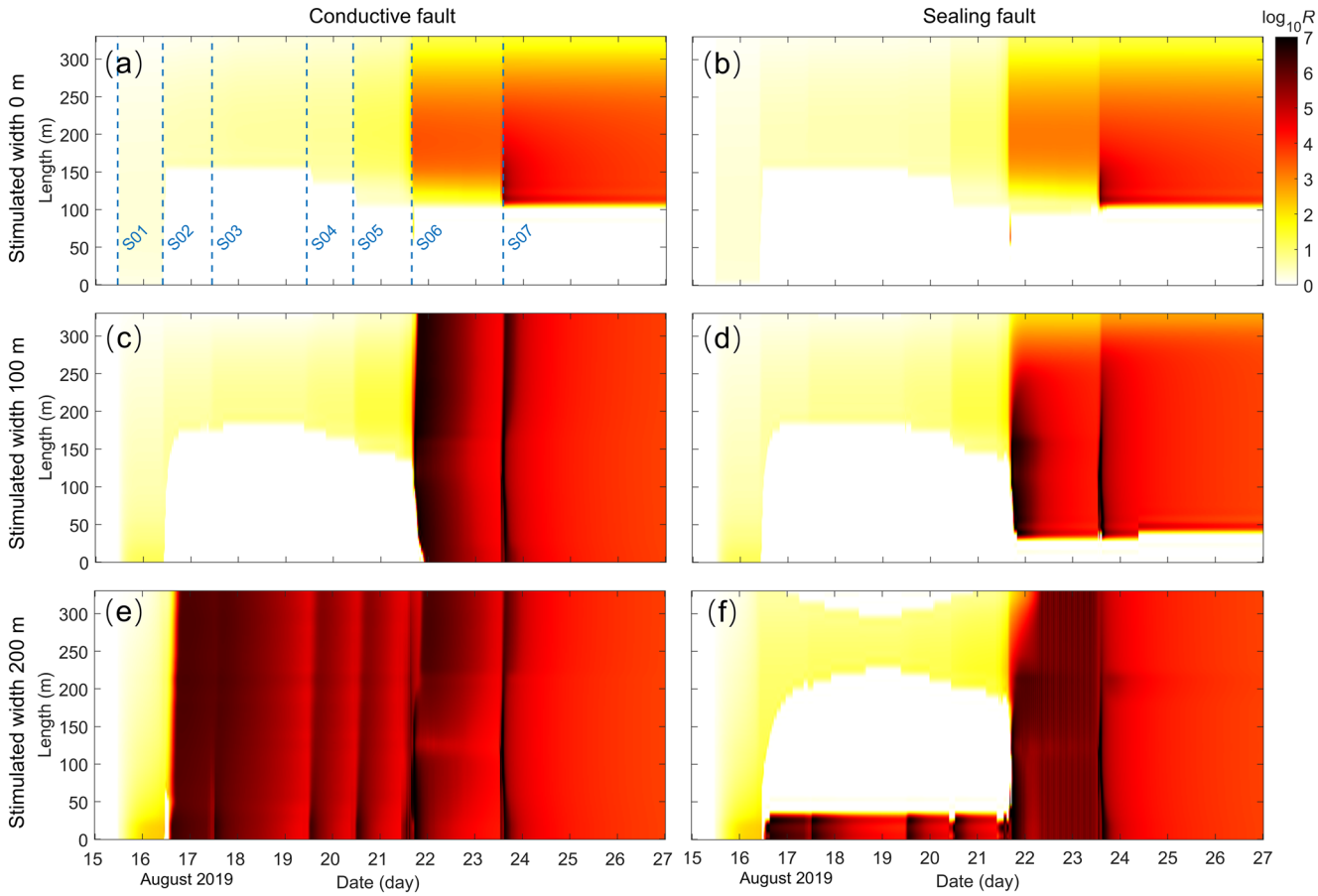

Figure 11. Evolution of seismicity rate R along the PNR-2 fault plane (the dashed purple line A-A in Figure 6a): (a) hydraulically isolated conductive fault, (b) hydraulically isolated sealing fault, (c) conductive fault hydraulically connected to the Eastern Zone, (d) sealing fault hydraulically connected to the Eastern Zone, (e) conductive fault hydraulically connected to both the NS and Eastern Zones, and (f) sealing fault hydraulically connected to both the NS and Eastern Zones.

model results are consistent with the conclusion of Segall and Lu (2015) that the pore pressure change dominates near the injector, whereas the poroelastic stresses are dominant at greater distance.

Figure 13c presents the mean seismicity rate R computed based on Coulomb failure stress change rate $\Delta\dot{\tau}$ (in solid lines) and pore pressure change rate $\Delta\dot{p}$ (in dashed lines) on the PNR-2 fault for the three conductive fault model scenarios (blue, orange and green colored for 0, 100, and 200 m stimulated widths, respectively). Figure 13d

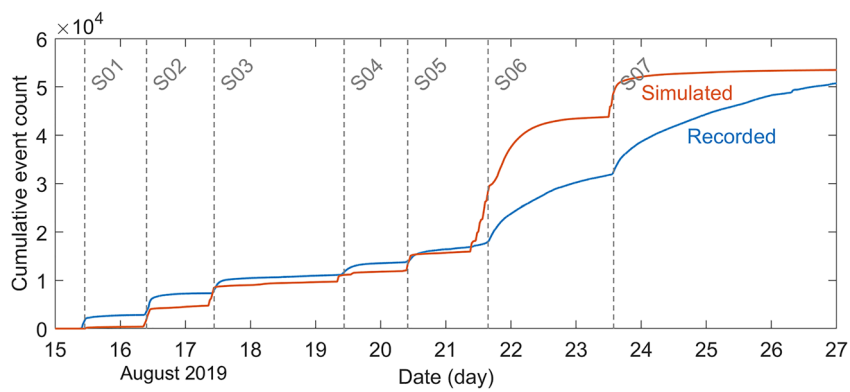

Figure 12. The recorded and modeled cumulative seismic event counts over the hydraulic fracturing operation period. The PNR-2 fault is conductive and hydraulically connected to the Eastern Zone in the model.

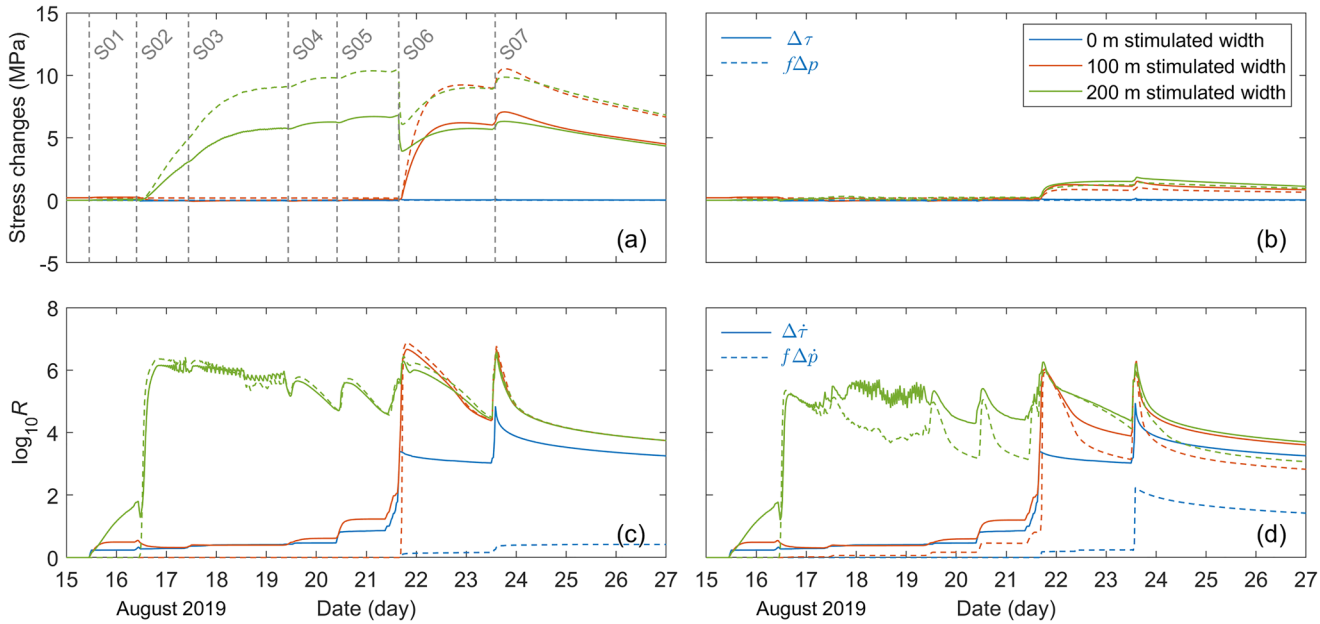

Figure 13. The contribution of pore pressure change to mean Coulomb stress change $\Delta\tau$ and seismicity rate R resolved on the PNR-2 fault. Mean Coulomb failure stress change $\Delta\tau$ and the contribution from pore pressure change $f\Delta p$ resolved on (a) a conductive fault, and (b) a sealing fault. Mean seismicity rate R calculated based on Coulomb failure stress change rate $\Delta\dot{\tau}$ and pore pressure change rate $\Delta\dot{p}$ on (c) a conductive fault, and (d) a sealing fault.

presents the same for the three sealing fault model scenarios. If the PNR-2 fault is conductive and hydraulically connected (orange and green lines, Figure 13c), the seismicity rate computed based on the Coulomb stress change rate $\Delta\dot{\tau}$ is slightly smaller than that based on pore pressure change rate $f\Delta\dot{p}$, due to the counteractive effect of poroelastic stressing. In contrast, the poroelastic stressing dominates and the opposite is true for a hydraulically isolated fault (blue lines, Figures 13a and 13b) or a sealing fault (all lines, Figure 13d).

In hydraulically connected scenarios (orange and green lines, Figure 13c), the seismicity rate within the PNR-2 fault jumps to high levels when the hydraulic connection is established at injection stage 6 for a stimulated width 100 m, and at stage 2 for a stimulated width 200 m, so as the seismicity rate computed based on pore pressure change rate $f\Delta\dot{p}$. In hydraulically isolated fault scenarios (blue lines, Figures 13c and 13d), the surge in the seismicity rate occurs when the poroelastic stress becomes prominent at injection stage 6, regardless of a conductive or sealing fault. The fault is subjected to minimal mean pore pressure disturbance in both scenarios, as shown in Figures 13a and 13b. Interestingly, in the former scenario (blue lines, Figure 13c), the increased pore pressure spreads across the fault plane leading to a gentle overall seismicity rate increase, but in the latter (blue lines, Figure 13d), the increased pore pressure is localized surrounding fracture tips, causing a relatively large seismicity rate increase even after being averaged across the full fault plane.

The heightened seismicity rate in hydraulically isolated fault scenarios demonstrates that the seismicity rate is very sensitive to the stress change rate. This sensitivity can also be observed by comparing seismicity rate within the fault after stage 1 in all the scenarios, which is purely attributed to poroelastic stressing. Depending on the poroelastic stressing influenced by different stimulated widths, the post-stage 1 seismicity rate within the fault is only $10^{0.33} = 2.1$ for a 0 m stimulated width, and $10^{0.55} = 3.5$ for a 100 m stimulated width, but could reach up to $10^{1.80} = 63$ for a 200 m stimulated width (Figures 13c and 13d).

5.2. Mechanism of the Post Shut-In M_L 2.9 Earthquake

Three plausible mechanisms examined for the occurrence of the post shut-in M_L 2.9 earthquake at the PNR site include the post shut-in pore pressure diffusion, poroelastic stressing on a non-overpressurized fault, and poroelastic stressing on an overpressurized fault. The first mechanism is represented by the conductive/sealing fault hydraulically connected to the Eastern Zone scenarios, the second by the hydraulically isolated conductive/sealing fault scenarios, and the last by the conductive/sealing fault hydraulically connected to both the NS and

Eastern Zones scenarios. We examined the possibility of the three mechanisms in terms of four factors based on modeling results: (a) Coulomb stress change, (b) seismicity rate, (c) timing of fault slippage, and (d) rupture area.

A Coulomb failure stress change in excess of the generalised triggering threshold of 0.01–0.1 MPa is considered to have high potential to trigger fault slippage (Kettlety & Verdon, 2021; Shapiro et al., 1997). Although Coulomb failure stress changes in the hydraulically isolated fault scenarios are much lower, they could reach well above 1 MPa ahead of fracture tips after stages 6 and 7 (Figure 9a). Therefore, none of three mechanisms could be ruled out in terms of the Coulomb stress change value. Nevertheless, the focus lies in whether the fault slippage criterion is satisfied after injection at the PNR field conditions, equivalently, whether the maximum Coulomb failure stress change within the fault occurs after injection at the PNR field conditions. Under constant injection rate conditions, following shut-in an unfavorably oriented, hydraulically connected fault may experience rapidly increased normal and shear stress changes, both contributing to the destabilization of the fault, before the pore pressure declines (Segall & Lu, 2015). This would result in a rapid increase of Coulomb stress, and thus a post-injection spike in seismicity rate. Even after the pore pressure begins to decline after shut-in, the combined action of rapid poroelastic stress changes and the delayed response of pore pressure may cause a post shut-in peak in Coulomb stress. In this case, the fault transmissivity plays a crucial role on the peak magnitude and duration of the post-injection increase in Coulomb stress (Wassing et al., 2021). A conductive fault, with a fast post-injection pore pressure decline, tends to have a small and narrow peak in Coulomb stress. In contrast, a sealing fault, with a slow post-injection pore pressure decline, could have a prominent and prolonged increase in Coulomb stress. It is noteworthy that the post-injection increase in Coulomb stress does not necessarily emerge across the full fault plane, but occur in a localized fault section. At the PNR hydraulic fracturing site, when the PNR-2 fault is hydraulically connected to the hydraulic fracture zones, its pore pressure change can be well constrained by the field-recorded wellhead pressure history. Under such conditions, the Coulomb failure stress change $\Delta\tau$ generated keeps decreasing after injection stage 7 at both points B and C (Figures 9c–9f), suggesting that the release of the normal stress is not rapid enough to cause a post-injection peak in the Coulomb stress. This indicates that although the poroelastic stressing mechanism is active, it does not play a governing role in triggering the post shut-in M_L 2.9 earthquake.

Seismicity rate allows more straightforward comparison between recorded and modeled event counts. Examination of seismicity rate indicates that all the three mechanisms could result in heightened seismicity rates over the majority of the PNR-2 fault plane (Figure 10). However, the seismicity rate estimated for hydraulically isolated fault scenarios is mostly below 10^4, while that for hydraulically connected fault scenarios can reach above 10^6. The field observation of the surge in event count surrounding the fault plane indicates that the poroelastic stressing on a non-overpressurized fault mechanism is less favorable.

The timing of post shut-in fault slippage differs for different mechanisms. For the poroelastic stressing on a non-overpressurized fault mechanism, the maximum Coulomb stress change occurs instantaneously when injection ceases, followed by a monotonical decline. For the post shut-in pore pressure diffusion mechanism, fault slippage usually happens sometime after the end of injection, depending on the permeability of the hydraulically connected fault. For the poroelastic stressing on an overpressurized fault mechanism, the delayed occurrence of fault slippage is also possible. The time after shut-in depends on the relative decline rate of pore pressure and normal stress, again modulated by the fault permeability (Wassing et al., 2021). Field records at the PNR site showed that the seismic magnitude began to increase around 5 hr after the end of injection. Before the M_L 2.9 event occurring over 60 hr post shut-in, there was an M_L 1.1 event around 9 hr post shut-in, an M_L 0.5 event around 14 hr post shut-in, and an M_L 2.1 event around 33 hr post shut-in. These observations indicate that the triggering mechanism was active over a prolonged period, thus at least the poroelastic stressing on a non-overpressurized fault mechanism could be ruled out.

Comparison between the field-derived rupture area and regions with positive modeled Coulomb stress change provides useful constraints on the underlying triggering mechanism. For the PNR site, of particular interest is the distribution of recorded seismicity around the poroelastic clamped fault section: recorded seismicity within this fault section would suggest that the PNR-2 fault is conductive and hydraulically connected, and seismic quiescence would suggest the opposite. Field recorded seismic events surrounding the poroelastic clamped fault section did not occur until after stage 6 (Figure 7c). This observation is consistent with model results of the conductive fault hydraulically connected to the Eastern Zone scenario, where the modeled Coulomb stress change remains negative in the clamped fault section immediately after stage 6, but becomes positive after stage 7

(Figures 7 and 7c of Kettlety & Verdon, 2021). To constrain the fault permeability, we further examined intermediate fault permeabilities of 1, 10^{-2}, and 10^{-4} mD, and found that a fault permeability of 1 mD could be sufficiently conductive to yield similar model results (see Text S3 and Figure S4 in Supporting Information S1). This suggests that the PNR-2 fault is likely to be conductive, which allows the gradually elevated pore pressure to activate the poroelastic clamped fault section.

It is noteworthy that the stimulated width and fault permeability used in the models may not accurately represent the field conditions, but provide reasonable upper and lower bounds for extreme scenarios of hydromechanical behavior. Building upon these modeling results and analyses, it is proposed that the occurrence of the post shut-in M_L 2.9 earthquake was a three-staged process: hydraulic fracturing operations first stimulated surrounding reservoir formations and propagated fracture tips along the maximum horizontal principal stress orientation. Fracture tips then reached and established hydraulic connection with the conductive PNR-2 fault, followed by gradual pore pressure diffusion to the fault through stimulated regions. After the injection ceased, the pore pressure was significantly lowered, but it remained higher than the in-situ pressure and continued to drive the diffusion across the majority of the fault plane, eventually triggering the fault slippage and the earthquake. In view of this mechanism, continuous microseismic and hydrogeological monitoring is recommended over a prolonged post shut-in period. In case of continuously increasing seismic magnitude of post shut-in events, flowback of injected fluids might be performed to lower overpressure and prevent the delayed occurrence of large induced earthquakes.

5.3. Simplification Considerations in Modeling Hydraulic Fracturing

The coupled model developed in this work considers key geological structures that are relevant to the fault slippage from a geomechanics perspective. However, the coupled model developed may not fully represent the complex geological conditions. In this model, uniform geomechanical and hydrological properties were used for shale formations within the model domain, without considering geological features other than the PNR-2 fault. The Bowland Basin where the PNR-2 site is located contains a gas-bearing shale gas section that extends across the north of England and is extremely thick (over 1.5 km thick, and ~1.2 km thick at the PNR-2 site) (Clarke, Soroush, & Wood, 2019; Kettlety et al., 2021). Interpretation of 3D seismic survey and wellbore observations indicated that the shale formations are comprised of Upper and Lower Bowland Shales (Andrews, 2013; Clarke, Soroush, & Wood, 2019). Although there are no reliable determination of intermediate bedding or fluid conduits within the shale formations, they are known to be intensely fractured which significantly adds to the heterogeneity. Comprehensive core sampling, rock mechanics testing, and field characterization programmes were conducted to obtain minerology and composition, and geomechanical and reservoir properties of Bowland shales (Clarke et al., 2018). The Upper and Lower Bowland shales can be distinguished in terms of lithology, log signatures and key zonal ammonoids. Gamma ray logging for the Lower Bowland Shale revealed more pronounced peaks, which correspond to higher Poisson's ratio, and lower Young's modulus and brittleness index. However, the overall control of lithology on geomechanical properties of the two shales is not significant. Laboratory-measured geomechanical properties of core samples from both the two shale units showed significant variation. Therefore, the coupled model could be further improved by better representing the geological and rock property variability of the Bowland Shale.

Proper representation of hydraulic stimulated regions is critical to the evaluation of the consequent induced seismicity. We have made several simplifications with regards to the incorporation of hydraulic fractures and associated stimulated regions for ease of modeling and interpretation. The model only implemented two major hydraulic fractures, although a swarm of seismic events also occurred in other regions (such as the Western Cluster). The structure corresponding to the Western Cluster was considered less significant from the perspective of fault reactivation and not modeled in this work, since the cluster was distant from the PNR-2 fault and it did not connect to any significant seismogenic features. Another simplification is that we used a uniform stimulated width around the two major hydraulic fractures, assuming that hydraulic fracture branches produced are evenly distributed around major fractures. The range of stimulated widths used was estimated based on the spatial distribution of field recorded microseismicity at the PNR site, which were usually located within 100 m distance to major hydraulic fractures (Figure 1). It is acknowledged that the uniform stimulated width may not be representative of the reality, as hydraulic stimulation may propagate in preferential directions associated with the in-situ stress and geological conditions (e.g., Li et al., 2015).

In the present work, we do not explicitly solve fracture dynamics of the hydraulic fracturing process, but rather examine the fluid pressure conditions resulting from the fracture dynamics. It is acknowledged that the development of explicit fracture dynamics-based numerical modeling approaches to model fracture propagation is an integral part of analysis of stimulation operations. For such modeling approaches, the methods by which the fracture propagation is handled and the fracture front is resolved is pivotal to the accuracy of model solutions (Chen et al., 2021; Lecampion et al., 2018). One family of numerical methods is based on linear elastic fracture mechanics (LEFM) and tracks the fracture front either explicitly or implicitly. Another family of numerical methods resolves the location of fracture front up to the spatial discretization size. This family includes finite element models incorporating cohesive zones and meso-scale models (such as discrete element models). These modeling approaches enable the simulation of physical processes associated with the fracturing itself, and might therefore be expected to recreate more realistic fracture geometries. However, both families of modeling approaches require fine mesh discretization to accurately capture the fracture process zone, which presents a significant challenge that impedes their application to solve 3D engineering-scale problems. In this sense, engineering models that make additional assumptions to reduce computational cost are preferred to enable practical engineering design and analysis (Lecampion et al., 2018).

The focus of this work is to realistically represent the hydrofracturing-induced fluid pressure distribution following the field-derived hydraulic fracture geometry, rather than to capture the physical process of hydraulic fracturing (such as fracture propagation and interaction). It is essential for the model to reproduce field-derived hydraulic fracture propagation behavior, as it influences the spatiotemporal distribution of fluid pressure and consequently the timing of fault instability. However, the field observed hydraulic fracture propagation is influenced by various uncertain factors such as the heterogeneity in rock properties and the existence of natural fractures, and it is difficult to directly use fracture dynamics-based modeling approaches to represent the field hydraulic fracture propagation behavior in terms of fracture dimensions (length and width) and fracture propagation velocity. The method used in this work models the fracturing-induced fluid pressure distribution through applying injection pressure on activated segments of pre-defined fracture geometries that are well constrained by field observations of the microseismicity. The time-varying pressure distribution is reflected by the progressive activation of field-derived hydraulic fractures, representing a first-order approximation to the field-derived propagating hydraulic fracture length. Therefore, it is believed that this modeling approach is suitable to reproduce the fluid pressure distribution associated with hydraulic fracturing.

6. Conclusions

A 3D fully coupled poroelastic model was developed to simulate the hydromechanical response of the shale reservoir formation embedded with the 330 m long, 250 m high PNR-2 fault during and after a one-week period of hydraulic fracturing operations in August 2019 at the PNR site, UK. Based on the stress and pore pressure modeled, the slippage potential of the PNR-2 fault responsible for the post shut-in M_L 2.9 earthquake was evaluated in terms of the Coulomb failure stress change and seismicity rate. A total of six model scenarios, considering various fault permeabilities and hydraulic connection between injection regions and faults, were modeled to identify the causal mechanism amongst three hypotheses, that is, the post shut-in pore pressure diffusion, poroelastic stressing on a non-overpressurized fault, and poroelastic stressing on an overpressurized fault.

Coupled modeling results have shown that increased pore pressure plays a dominant role in triggering the fault slippage, although the poroelastic stress may have acted to promote the slippage. Amongst the three plausible mechanisms, the post shut-in pore pressure diffusion is the most favored in terms of Coulomb stress change, seismicity rate, timing of fault slippage and rupture area. Comparison between various model scenarios has indicated that the occurrence of the post shut-in M_L 2.9 earthquake was a three-staged process, where hydraulic fractures first stimulated surrounding reservoir formations, then hydraulically connected to the conductive PNR-2 fault that allowed gradual pore pressure diffusion, and eventually the fault was activated primarily under the direct increase in pore pressure.

Model results also highlighted the paramount role of the hydraulic connectivity of faults to injection regions and fault permeability in promoting fault rupture, in addition to the fault orientation with respect to the ambient stress field. The hydraulic connectivity of faults to injection regions and fault permeability have the largest impact on resolved stress changes and consequently seismicity rate, by moderating the overpressure applied on fault planes.

In comparison to the direct effect of elevated fluid pressure, the poroelastic stressing is less significant although it does play a role in changing the stress changes and seismicity rate. Co-seismic activation of faults of the same orientation may be attributed to different triggering mechanisms in different hydrogeological settings and stimulation conditions.

Appendix A: Governing Equations of Poroelasticity

The theory of linear poroelasticity has been used to describe the hydromechanical behavior of porous media such as subsurface rocks (Wang, 2017). The poroelastic constitutive equations consist of a set of six equations that describe the solid deformation as a function of the stress and pore pressure, and an equation that describes the pore fluid mass related to the pore pressure and mean stress. The first set of constitutive equations for an isotropic, linear elastic porous medium relate the strains ε_{ij} to the stresses σ_{ij} and pore pressure p:

$$\varepsilon_{ij} = \frac{1}{2G}\left[\sigma_{ij} - \frac{\nu}{1+\nu}\sigma_{kk}\delta_{ij}\right] + \frac{\alpha}{3K}p\delta_{ij} \tag{A1}$$

where ν, K, and G are Poisson's ratio, bulk modulus and shear modulus of the porous medium, respectively, α is the Biot's coefficient, and δ_{ij} is the Kronecker delta.

The other constitutive equation relates the increment of fluid content ζ to the pore pressure p and mean normal stress $\sigma_{kk}/3$:

$$\zeta = \frac{\alpha}{K}\frac{\sigma_{kk}}{3} + \frac{\alpha}{KB}p \tag{A2}$$

where B is the Skempton's coefficient.

The geomechanical deformation of the poroelastic medium is based on stress equilibrium expressed in terms of the linear momentum balance equations:

$$\sigma_{ij,j} + f_i = 0 \tag{A3}$$

where f_i is the body force. The effective stress σ'_{ij} is defined by the stress σ_{ij} and pore pressure p:

$$\sigma'_{ij} = \sigma_{ij} + \alpha p\delta_{ij} \tag{A4}$$

By substituting Equation A1 and considering the compatibility relations between the strain and displacement $\varepsilon_{ij} = \frac{1}{2}(u_{i,j} + u_{j,i})$, the stress equilibrium equations can be expressed in terms of the displacement:

$$G\nabla^2 u_i + \frac{G}{1-2v}\frac{\partial^2 u_j}{\partial x_i \partial x_j} - \alpha\frac{\partial p}{\partial x_i} + f_i = 0 \tag{A5}$$

The fluid flow in the porous medium is described by the mass conservation equation:

$$\frac{\partial \zeta}{\partial t} + \frac{\partial q_i}{\partial x_i} = Q \tag{A6}$$

where q_i is the flux of fluid flow, and Q is a fluid mass source. Darcy's law for fluid flow in porous medium takes the form:

$$q_i = -\frac{k}{\mu}\frac{\partial p}{\partial x_i} \tag{A7}$$

where k is the permeability of rocks, and μ is the fluid viscosity. Substituting Equations A2 and A7 to Equation A6 gives:

$$\frac{\alpha}{KB}\left(\frac{B}{3}\frac{\partial \sigma_{kk}}{\partial t} + \frac{\partial p}{\partial t}\right) - \frac{k}{\mu}\frac{\partial^2 p}{\partial x_i^2} = Q \tag{A8}$$

The linear poroelasticity of the medium involves the two-way coupling between stress and fluid flow. Both coupling terms are implemented in the constitutive equations: the fluid-to-solid coupling is reflected in the

influence of the pore pressure on the strain (Equation A1), and the solid-to-fluid coupling is considered by the influence of the mean normal stress on the fluid mass (Equation A2). The coupled poroelastic response could be simulated by solving the governing equations of geomechanics and fluid flow incorporating these constitutive relations.

Appendix B: Coulomb Failure Stress Change

The potential for fracture slippage can be evaluated by the Coulomb failure stress change along fracture planes:

$$\Delta\tau = \Delta\tau_s + f(\Delta\sigma_n + \Delta p) \tag{B1}$$

where f is the friction coefficient, and $\Delta\sigma_n$ and $\Delta\tau_s$ are normal and shear stress changes resolved on the fracture plane, respectively. Here, negative normal stress changes $\Delta\sigma_n$ indicate rock compression. The potential for fracture slippage is elevated for a positive Coulomb failure stress change, and suppressed for a negative value. To isolate respective contributions of poroelastic stressing and pore pressure change, Equation B1 can be re-arranged in terms of poroelastic stress change and pore pressure change:

$$\Delta\tau = (\Delta\tau_s + f\Delta\sigma_n) + f\Delta p \tag{B2}$$

Appendix C: Seismicity Rate Model

Dieterich (1994) developed a model to quantify the rate of earthquake occurrence based on the assumption that the timing of a sequence of earthquake nucleation events is controlled by the initial conditions of nucleation sources and the stressing history. Implementation of the model to the nucleation of accelerating slip on faults with the rate-and-state friction law yields a state-variable constitutive formulation of seismicity rate associated with the applied stressing history. Segall and Lu (2015) re-formulated the seismicity rate framework by eliminating the state variable and expressing the equation in terms of the seismicity rate relative to the background rate R:

$$\frac{dR}{dt} = \frac{R}{t_a}\left(\frac{\dot{\tau}}{\dot{\tau}_0} - R\right) \tag{C1}$$

where $\dot{\tau}$ is the Coulomb stressing rate, $\dot{\tau}_0$ is the tectonic Coulomb stressing rate, and $t_a = a\bar{\sigma}/\dot{\tau}_0$ is a characteristic decay time. a is the constitutive parameter reflecting the slip rate effect in the rate-and-state friction law. $\bar{\sigma}$ is the in-situ effective normal stress. For any given Coulomb stressing rate, there is a steady-state seismicity rate $R_{ss} = \dot{\tau}/\dot{\tau}_0$. This implies that an arbitrarily low tectonic stressing rate could cause a low background seismicity rate.

Data Availability Statement

Operations data at the PNR2 well presented here are available from the Oil and Gas Authority (https://www.ogauthority.co.uk/exploration-production/onshore/onshore-reports-and-data/preston-new-road-well-pnr2-data-studies/).

Acknowledgments
The first author would like to thank the Open Research Fund of the Key Laboratory of Deep Earth Science and Engineering, Sichuan University (Grant No: DESE 202101) for their support of this research. The second author is supported by the NERC UK Unconventional Hydrocarbon Challenge Grants (Grant No: NE/R018006/1 and NE/R018162/1). The authors gratefully acknowledge the constructive reviews by Jeremy Maurer, an anonymous reviewer and an anonymous Associate Editor which improved the quality of this manuscript.

References

Albaric, J., Oye, V., Langet, N., Hasting, M., Lecomte, I., Iranpour, K., et al. (2014). Monitoring of induced seismicity during the first geothermal reservoir stimulation at Paralana, Australia. *Geothermics*, *52*, 120–131. https://doi.org/10.1016/j.geothermics.2013.10.013

Andrews, I. J. (2013). *The Carboniferous Bowland Shale gas study: Geology and resource estimation*.

Atkinson, G. M., Eaton, D. W., & Igonin, N. (2020). Developments in understanding seismicity triggered by hydraulic fracturing. *Nature Reviews Earth & Environment*, *1*(5), 264–277. https://doi.org/10.1038/s43017-020-0049-7

Baisch, S., Vörös, R., Rothert, E., Stang, H., Jung, R., & Schellschmidt, R. (2010). A numerical model for fluid injection induced seismicity at Soultz-sous-Forêts. *International Journal of Rock Mechanics and Mining Sciences*, *47*(3), 405–413. https://doi.org/10.1016/j.ijrmms.2009.10.001

Cao, N.-T., Eisner, L., & Jechumtálová, Z. (2020). Next record breaking magnitude for injection induced seismicity. *First Break*, *38*(2), 53–57. https://doi.org/10.3997/1365-2397.fb2020010

Cao, W., Shi, J.-Q., Durucan, S., & Korre, A. (2021). Evaluation of shear slip stress transfer mechanism for induced microseismicity at in Salah CO_2 storage site. *International Journal of Greenhouse Gas Control*, *107*. https://doi.org/10.1016/j.ijggc.2021.103302

Chang, K. W., & Segall, P. (2016). Injection-induced seismicity on basement faults including poroelastic stressing. *Journal of Geophysical Research: Solid Earth*, *121*(4), 2708–2726. https://doi.org/10.1002/2015jb012561

Chang, K. W., Yoon, H., & Martinez, M. J. (2018). Seismicity rate surge on faults after shut-in: Poroelastic response to fluid injection. *Bulletin of the Seismological Society of America*, *108*(4), 1889–1904. https://doi.org/10.1785/0120180054

Chen, B., Barboza, B. R., Sun, Y., Bai, J., Thomas, H. R., Dutko, M., et al. (2021). A review of hydraulic fracturing simulation. *Archives of Computational Methods in Engineering*, 1–58. https://doi.org/10.1007/s11831-021-09653-z

Clarke, H., Eisner, L., Styles, P., & Turner, P. (2014). Felt seismicity associated with shale gas hydraulic fracturing: The first documented example in Europe. *Geophysical Research Letters*, *41*(23), 8308–8314. https://doi.org/10.1002/2014gl062047

Clarke, H., Soroush, H., & Wood, T. (2019). Preston New Road: The role of geomechanics in successful drilling of the UK's first horizontal shale gas well. In *SPE Europec featured at 81st EAGE conference and exhibition*.

Clarke, H., Turner, P., Bustin, R. M., Riley, N., & Besly, B. (2018). Shale gas resources of the Bowland Basin, NW England: A holistic study. *Petroleum Geoscience*, *24*(3), 287–322. https://doi.org/10.1144/petgeo2017-066

Clarke, H., Verdon, J. P., Kettlety, T., Baird, A. F., & Kendall, J.-M. (2019). Real-time imaging, forecasting, and management of human-induced seismicity at Preston New Road, Lancashire, England. *Seismological Research Letters*, *90*(5), 1902–1915. https://doi.org/10.1785/0220190110

De Simone, S., Carrera, J., & Vilarrasa, V. (2017). Superposition approach to understand triggering mechanisms of post-injection induced seismicity. *Geothermics*, *70*, 85–97. https://doi.org/10.1016/j.geothermics.2017.05.011

Dieterich, J. (1994). A constitutive law for rate of earthquake production and its application to earthquake clustering. *Journal of Geophysical Research*, *99*(B2), 2601–2618. https://doi.org/10.1029/93jb02581

Elsworth, D., Spiers, C. J., & Niemeijer, A. R. (2016). Understanding induced seismicity. *Science*, *354*(6318), 1380–1381. https://doi.org/10.1126/science.aal2584

Evans, K. F., Moriya, H., Niitsuma, H., Jones, R. H., Phillips, W. S., Genter, A., et al. (2005). Microseismicity and permeability enhancement of hydrogeologic structures during massive fluid injections into granite at 3 km depth at the Soultz HDR site. *Geophysical Journal International*, *160*(1), 388–412.

Eyre, T. S., Eaton, D. W., Garagash, D. I., Zecevic, M., Venieri, M., Weir, R., & Lawton, D. C. (2019). The role of aseismic slip in hydraulic fracturing–induced seismicity. *Science Advances*, *5*(8), eaav7172. https://doi.org/10.1126/sciadv.aav7172

Eyre, T. S., Zecevic, M., Salvage, R. O., & Eaton, D. W. (2020). A long-lived swarm of hydraulic fracturing-induced seismicity provides evidence for aseismic slip. *Bulletin of the Seismological Society of America*, *110*(5), 2205–2215. https://doi.org/10.1785/0120200107

Grigoli, F., Cesca, S., Rinaldi, A. P., Manconi, A., Lopez-Comino, J. A., Clinton, J. F., et al. (2018). The November 2017 M_w 5.5 Pohang earthquake: A possible case of induced seismicity in South Korea. *Science*, *360*(6392), 1003–1006. https://doi.org/10.1126/science.aat2010

Guglielmi, Y., Cappa, F., Avouac, J.-P., Henry, P., & Elsworth, D. (2015). Seismicity triggered by fluid injection–induced aseismic slip. *Science*, *348*(6240), 1224–1226. https://doi.org/10.1126/science.aab0476

Hager, B. H., Dieterich, J., Frohlich, C., Juanes, R., Mantica, S., Shaw, J. H., et al. (2021). A process-based approach to understanding and managing triggered seismicity. *Nature*, *595*(7869), 684–689. https://doi.org/10.1038/s41586-021-03668-z

Häring, M. O., Schanz, U., Ladner, F., & Dyer, B. C. (2008). Characterisation of the Basel 1 enhanced geothermal system. *Geothermics*, *37*(5), 469–495.

Hsieh, P. A., & Bredehoeft, J. D. (1981). A reservoir analysis of the Denver earthquakes: A case of induced seismicity. *Journal of Geophysical Research*, *86*(B2), 903–920. https://doi.org/10.1029/jb086ib02p00903

Kettlety, T., & Verdon, J. P. (2021). Fault Triggering mechanisms for hydraulic fracturing-induced seismicity from the Preston New Road, UK case study. *Frontiers in Earth Science*, *9*, 382. https://doi.org/10.3389/feart.2021.670771

Kettlety, T., Verdon, J. P., Butcher, A., Hampson, M., & Craddock, L. (2021). High-resolution imaging of the ML 2.9 August 2019 earthquake in Lancashire, United Kingdom, induced by hydraulic fracturing during Preston New Road PNR-2 operations. *Seismological Society of America*, *92*(1), 151–169. https://doi.org/10.1785/0220200187

Kettlety, T., Verdon, J. P., Werner, M. J., & Kendall, J.-M. (2020). Stress transfer from opening hydraulic fractures controls the distribution of induced seismicity. *Journal of Geophysical Research: Solid Earth*, *125*(1), e2019JB018794. https://doi.org/10.1029/2019jb018794

Kwiatek, G., Saarno, T., Ader, T., Bluemle, F., Bohnhoff, M., Chendorain, M., et al. (2019). Controlling fluid-induced seismicity during a 6.1-km-deep geothermal stimulation in Finland. *Science Advances*, *5*(5), eaav7224. https://doi.org/10.1126/sciadv.aav7224

Lecampion, B., Bunger, A., & Zhang, X. (2018). Numerical methods for hydraulic fracture propagation: A review of recent trends. *Journal of Natural Gas Science and Engineering*, *49*, 66–83. https://doi.org/10.1016/j.jngse.2017.10.012

Lei, X., Wang, Z., & Su, J. (2019). The December 2018 ML 5.7 and January 2019 ML 5.3 earthquakes in South Sichuan basin induced by shale gas hydraulic fracturing. *Seismological Research Letters*, *90*(3), 1099–1110. https://doi.org/10.1785/0220190029

Li, Q., Xing, H., Liu, J., & Liu, X. (2015). A review on hydraulic fracturing of unconventional reservoir. *Petroleum*, *1*(1), 8–15. https://doi.org/10.1016/j.petlm.2015.03.008

McClure, M. W. (2015). Generation of large postinjection-induced seismic events by backflow from dead-end faults and fractures. *Geophysical Research Letters*, *42*(16), 6647–6654. https://doi.org/10.1002/2015gl065028

McClure, M. W., & Horne, R. N. (2011). Investigation of injection-induced seismicity using a coupled fluid flow and rate/state friction model. *Geophysics*, *76*(6), WC181–WC198. https://doi.org/10.1190/geo2011-0064.1

McGarr, A. (2014). Maximum magnitude earthquakes induced by fluid injection. *Journal of Geophysical Research: Solid Earth*, *119*(2), 1008–1019. https://doi.org/10.1002/2013jb010597

Parotidis, M., Shapiro, S. A., & Rothert, E. (2004). Back front of seismicity induced after termination of borehole fluid injection. *Geophysical Research Letters*, *31*(2). https://doi.org/10.1029/2003gl018987

Rahman, M. M., & Rahman, M. K. (2010). A review of hydraulic fracture models and development of an improved pseudo-3D model for stimulating tight oil/gas sand. *Energy Sources, Part A: Recovery, Utilization, and Environmental Effects*, *32*(15), 1416–1436. https://doi.org/10.1080/15567030903060523

Schoenball, M., Baujard, C., Kohl, T., & Dorbath, L. (2012). The role of triggering by static stress transfer during geothermal reservoir stimulation. *Journal of Geophysical Research*, *117*(B9). https://doi.org/10.1029/2012jb009304

Schultz, R., Skoumal, R. J., Brudzinski, M. R., Eaton, D., Baptie, B., & Ellsworth, W. (2020). Hydraulic fracturing-induced seismicity. *Reviews of Geophysics*, *58*(3), e2019RG000695. https://doi.org/10.1029/2019rg000695

Segall, P. (1989). Earthquakes triggered by fluid extraction. *Geology*, *17*(10), 942–946. https://doi.org/10.1130/0091-7613(1989)017<0942:etbfe>2.3.co;2

Segall, P., & Lu, S. (2015). Injection-induced seismicity: Poroelastic and earthquake nucleation effects. *Journal of Geophysical Research: Solid Earth*, *120*(7), 5082–5103. https://doi.org/10.1002/2015jb012060

Shapiro, S. A., Huenges, E., & Borm, G. (1997). Estimating the crust permeability from fluid-injection-induced seismic emission at the KTB site. *Geophysical Journal International*, *131*(2), F15–F18. https://doi.org/10.1111/j.1365-246x.1997.tb01215.x

Si, G., Cai, W., Wang, S., & Li, X. (2020). Prediction of relatively high-energy seismic events using spatial–temporal parametrisation of mining-induced seismicity. *Rock Mechanics and Rock Engineering*, *53*, 1–22. https://doi.org/10.1007/s00603-020-02210-3

Talwani, P., & Acree, S. (1985). Pore pressure diffusion and the mechanism of reservoir-induced seismicity. In *Earthquake prediction* (pp. 947–965). Springer. https://doi.org/10.1007/978-3-0348-6245-5_14

Ucar, E., Berre, I., & Keilegavlen, E. (2017). Postinjection normal closure of fractures as a mechanism for induced seismicity. *Geophysical Research Letters*, *44*(19), 9598–9606. https://doi.org/10.1002/2017gl074282

Verdon, J. P., & Bommer, J. (2021). Green, yellow, red, or out of the blue? An assessment of Traffic light schemes to mitigate the impact of hydraulic fracturing-induced seismicity. *Journal of Seismology*, *25*, 1–26. https://doi.org/10.1007/s10950-020-09966-9

Verdon, J. P., & Budge, J. (2018). Examining the capability of statistical models to mitigate induced seismicity during hydraulic fracturing of shale gas reservoirs. *Bulletin of the Seismological Society of America*, *108*(2), 690–701. https://doi.org/10.1785/0120170207

Verdon, J. P., Kettlety, T., & Kendall, J.-M. (2020). *Geomechanical interpretation of induced seismicity at the Preston New Road PNR-2 Well*. Lancashire.

Wang, H. F. (2017). *Theory of linear poroelasticity with applications to geomechanics and hydrogeology*. Princeton University Press.

Wang, J., Li, T., Gu, Y. J., Schultz, R., Yusifbayov, J., & Zhang, M. (2020). Sequential fault reactivation and secondary triggering in the March 2019 Red Deer induced earthquake swarm. *Geophysical Research Letters*, *47*(22), e2020GL090219. https://doi.org/10.1029/2020gl090219

Wassing, B. B. T., Gan, Q., Candela, T., & Fokker, P. A. (2021). Effects of fault transmissivity on the potential of fault reactivation and induced seismicity: Implications for understanding induced seismicity at Pohang EGS. *Geothermics*, *91*, 101976. https://doi.org/10.1016/j.geothermics.2020.101976

Zeng, Y., Lei, Q., Wang, Z., Ding, S., Liu, K., Huang, X., et al. (2021). Numerical simulation of fluid injection-induced fault slip in heterogeneous shale formations. *Computers and Geotechnics*, *134*, 104120. https://doi.org/10.1016/j.compgeo.2021.104120